Verification of I-131 Yield from the Neutron Irradiation of Tellurium

A Thesis Presented for the

Master of Science

Degree

The University of Tennessee, Knoxville

Robert Christopher Haffner

May 2018

Acknowledgments

This project and my studies would not be possible without the financial support and flexibility of my employer, POWER Engineers (Sega, Inc.). In particular, I would like to thank my former department manager, Steve Wopata, for the kind and motivational support of which I was often reminded–not to screw it up or embarrass him when leaving the office. I also greatly appreciate the support I received from Dr. Miller at MURR, who provided a part-time position for me that introduced me to this project during a time of academic uncertainty and instability at the University of Missouri. He continued to supply answers to my many questions long after I accepted a full-time position at Sega. I would also like to thank Dr. Lukosi who was understanding of my interesting predicament and agreed to be my advisor on this thesis project. Lastly, I would like to thank my wife who endured the many long hours I spent studying and working as a distance student and full-time engineer.

Abstract

Radioactive isotopes of iodine have many uses in modern medicine due to the thyroid gland's affinity for iodine. The University of Missouri Research Reactor (MURR) plans to begin commercial production of iodine-131 (I-131) via the neutron irradiation of tellurium-130 (Te-130) and the subsequent beta decays of the products of the neutron absorption reaction, Te-131 and Te-131m. However, various discrepancies in literature and nuclear databases regarding a range of system parameters have convoluted the expected I-131 yield. In this work, a model constructed by integrating a system of one-group, nuclide-activation, differential rate equations to acquire analytical solutions to the number of atoms of each nuclide during activation formulated a more accurate calculation of the I-131 yield. To obtain the integrated result, the model linearized the equations in matrix form via the Laplace transform before solving them by employing Gaussian elimination. Cauchy's residue theorem was finally applied to this result to acquire the inverse Laplace transforms. These symbolic analytical solutions were left as functions of the user's desired parameters and formed a non-linear regression problem between the model's equations and experimental data provided by MURR, which the Gauss-Newton method determined the best-fit parameters for in a Monte Carlo analysis. A functional estimate for the thermal Te-130 neutron absorption cross-section was determined to be approximately 0.127 ± 0.007 barns for a 170.7 g natural tellurium target. The fractional yield of Te-131 resulting from the neutron absorption of Te-130 followed a normal distribution with a mean and standard deviation of 0.960 ± 0.003. These best fit parameters and the model were then validated against additional experimental data provided by MURR. Finally, the optimal cooling time of the sample to acquire the maximum I-131 activity did not exceed 3.87 ± 0.02 hours.

Table of Contents

List of Tables

List of Figures

Chapter 1

Background and Introduction

Iodine-131 (I-131) is an unstable isotope of iodine that decays via beta particle emission with a half-life of 8.0252 days. Hospitals and medical professionals utilize I-131 as a tracer for medical imaging and regularly to treat patients that suffer from hyperactive thyroids and certain types of thyroid cancer. Since I-131 decays at an expedient rate, it is important for the end-users to have a reliable and consistent supply of I-131 packed with a high specific activity to treat their patients. The University of Missouri Research Reactor (MURR) plans to begin domestic production of this isotope within the next year to satisfy these necessary demands of the medical industry.

1.1 Medical Uses of Iodine-131

Thyrotoxicosis is a generic term for the condition that occurs due to the excessive production of thyroid hormones thyroxine (T4) and triiodothyronine (T3), whereas hyperthyroidism indicates an overactive thyroid that results in thyrotoxicosis. Autoimmune hyperthyroidism–often referred to as Graves Disease–represents 70-80% of the cases of hyperthyroidism and effects an overwhelmingly larger percentage of women than men with prevalences of 19 per 1000 for females and less than 1 per 1000 in males, [23].

There are typically three options a patient can consider to treat thyrotoxicosis: surgery (thyroidectomy), drug therapy, or radioactive iodine (RAI). A thyroidectomy can cause serious, unforeseeable complications and almost always results in hypothyroidism (the

inability of the thyroid to produce enough hormones), which must be managed with prescription medication for the remainder of the patient's life. Drug therapy utilizes medications that hinder the thyroid's ability to produce hormones. If the patient discontinues drug therapy, hyperthyroidism will more than likely return. Surgery and drug therapy successfully relieve thyrotoxicosis at rates of 80% and 50%, respectively, [19].

An alternative treatment option called radioactive iodine (RAI) utilizes a radioactive isotope of iodine (I-131) to destroy follicular cells in the thyroid. The thyroid has a predilection for iodine due to the role played by this chemical in the thyroid's synthesis of hormones, T3 and T4. As the follicular cells attach themselves to the unstable isotope, they are killed off by the radiation, thus reducing the thyroid's production of hormones and regulating hyperthyroidism. The uptake of I-131 by the thyroid is exceedingly high at approximately 25% 24 hours following ingestion of iodine and 15% after 56 hours following inhalation, [18]. The high uptake of iodine by the thyroid results in a very large radioactive dose directly to the organ and a small dose to the rest of the body. RAI also has a lower risk of hypothyroidism occurring in the patient following radiation therapy. RAI successfully relieves thyrotoxicosis at a rate of 90-95% and results in hypothyroidism in the patient 40-80% of the time, [19].

In addition to treating thyrotoxicosis, I-131 is used to treat papillary thyroid and follicular carcinoma, the two most prevalent types of thyroid cancer that represent approximately 90% of thyroid cancer cases, [9]. Thyroid cancer represents 3.5% of all new cancer cases in the United States (eleventh most common) with an estimated 56,870 new cases in 2017, [17]. Finally, I-131 is also regularly used as a tracer for medical imaging of the thyroid. Thus, the demand for I-131 is high in the medical industry.

1.2 Production

All nuclear reactors produce I-131 as a fission product of uranium-235 (U-235) with a yield abundance of 3.076%, according to [3]. However, extracting the iodine from spent nuclear fuel would require expensive and time consuming reprocessing in a sophisticated facility. Additionally, extracting only approximately 3% of the fuel would produce a large amount of

Table 1.1: Isotopic composition of natural tellurium with 95% confidence intervals, [20]

Isotope	Mass Abundance
Te-120	$0.00096 \pm 7 \times 10^{-6}$
Te-122	$0.0260 \pm 1 \times 10^{-5}$
Te-123	$0.00908 \pm 7 \times 10^{-6}$
Te-124	$0.0482 \pm 2 \times 10^{-5}$
Te-125	$0.0714 \pm 2 \times 10^{-5}$
Te-126	$0.1895 \pm 4 \times 10^{-5}$
Te-128	$0.3169 \pm 8 \times 10^{-5}$
Te-130	$0.3380 \pm 6 \times 10^{-5}$

nuclear waste. Given I-131's short half life (8.025 days), a large portion of the I-131 extracted from the processing may decay before it could be used.

However, a more practical alternative method to producing I-131 exists. I-131 is the daughter nuclide of the ground and metastable states of Te-131, which both beta decay into I-131. Te-130 has a relatively large thermal neutron absorption cross-section at 0.2 barns and has mole fraction of $0.3380 \pm 6.3 \times 10^{-5}$ (95% confidence interval) in natural tellurium as shown in Table 1.1, [20]. Although natural tellurium's abundance in the continental crust is rare with an average value similar to gold at 0.001 ppm according to [25], it is also produced as a byproduct from electrolytic copper refining. End users from solar, thermoelectric production, metallurgy, and rubber application industries utilize natural tellurium produced in this manner, [21]. Thus, raw natural tellurium is readily available and reasonably priced at \$35/pound for 99.95% tellurium (2016 data, [21]), although higher purities may be required for I-131 production and are likely more expensive.

The method of producing I-131 from the neutron capture products of Te-130 (Te-131 and Te-131m) is shown in Figure 1.1 and shown formally in Equations 1.1 through 1.5 below and is the process that the rest of this thesis will focus on. The contribution to I-131 from other tellurium isotopes apart from Te-130 is insignificant. Although this work assumes that Te-130 is stable, it actually beta decays into I-130, but the half-life is greater than 3.0×10^{24} years. Given the exceptionally long half-life and the insignificance of Te-130 decaying for I-131 production, the remainder of this work will assume Te-130 is stable.

$$ {}^{1}_{0}n + {}^{130}\,Te \rightarrow {}^{131}\,Te + \gamma \tag{1.1} $$

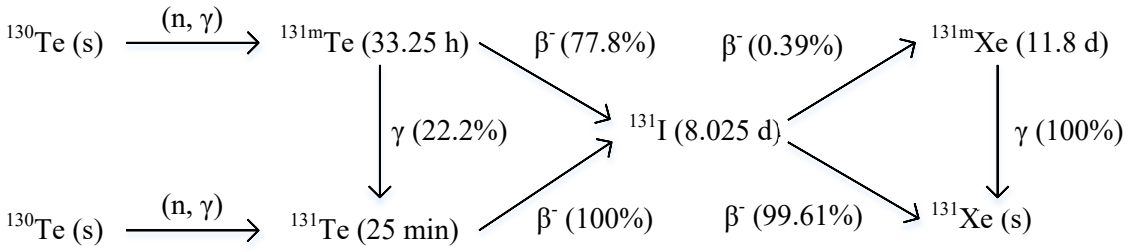

Figure 1.1: The irradiation and decay scheme of Te-130, Te-131, and I-131

$$^{1}_{0}n + ^{130}Te \rightarrow ^{131m}Te + \gamma \tag{1.2}$$

$$^{131}Te + ^{-1}e \rightarrow ^{131}I \tag{1.3}$$

$$^{131m}Te + ^{-1}e \rightarrow ^{131}I \tag{1.4}$$

$$^{131m}Te + \gamma \rightarrow ^{131}Te + ^{-1}e \rightarrow ^{131}I \tag{1.5}$$

Following irradiation, a facility can extract the I-131 from the rest of the natural tellurium target (and resulting products from irradiation) via a number of methods, the dry-distillation method being perhaps the easiest. This basic process consists of heating the irradiated sample–releasing the I-131–and subsequently capturing the I-131 in a sodium hydroxide (NaOH) solution.

1.3 Literature Review

Mathematical determinations of the final yield of I-131 produced via the process shown in Figure 1.1 varies widely in literature. Other discrepancies in literature surrounding this process include calculations for the optimal cooling time following irradiation to produce the maximum amount of I-131, the effect of various neutron fluxes on the yield and cooling time, the cross-sections of the nuclides involved (natural tellurium, Te-130, Te-131, Te-131m, and I-131), and the length of irradiation time to saturate the natural tellurium target with I-131.

Literature provides very little experimental data for the neutron absorption cross-sections (n,γ) of the nuclides involved with I-131 creation. There is no experimental data for Te-131

cross-sections, only one experimental data point for I-131 that has a very large uncertainty (51 ± 40, [24]), and various experimental and evaluated cross-sections that vary widely for Te-130, as shown in Table 1.2.

Table 1.2: Thermal cross-section discrepancies in literature

Reference	Type	Te-130 Cross-Section, barns
[3]	Evaluated	0.29
[1]	Evaluated	0.195
[2]	Evaluated	0.1862
[16]	Experimental	0.195 ± 0.01
[22]	Experimental	0.24 ± 0.02
[22]	Experimental	0.186 ± 0.013
[22]	Experimental	0.180 ± 0.019
[22]	Experimental	0.196 ± 0.023
[22]	Experimental	0.185 ± 0.028
[6]	Experimental	0.0147 ± 0.028
[10]	Experimental	0.193 ± 0.020

The cross-section of Te-130 is often explicitly stated for both the reactions in Equations 1.1 and 1.2–which can both be expressed as $^{130}\mathrm{Te}(n,\gamma)^{131}\mathrm{Te}$ and $^{130}\mathrm{Te}(n,\gamma)^{131m}\mathrm{Te}$, respectively–in the form of $0.2 + 0.04$. These two numbers represent the Te-130 cross-section that produces the Te-131 and Te-131m states, respectively, following a neutron absorption reaction.

In addition to the uncertainties in the Te-130 neutron absorption cross-section, the natural tellurium neutron absorption cross-section is also disputed. This is problematic because it greatly influences the neutron self-shielding effect (and coincidentally the neutron spectrum across the sample). Kochnov discussed the discrepancy in [13] where VisualBurnOut and ORIGEN-S (two different nuclear codes) calculated one-group constants and I-131 concentrations resulting from the neutron irradiation of tellurium in the WWR-c reactor core. For I-131 production at this facility, the reactor irradiates TeO_2 two different times for 100 hours at a power of 10 Mwt (megawatts thermal) and a neutron flux of 10^{14} $n{\cdot}cm^{-2}{\cdot}s^{-1}$. There is a 68 hour cooling period between the two irradiations that allows time

for cooling, fuel reloading, target positioning, and other operations. The sample remains in the core at its position during this time.

The publication in [13] discovered significant differences between calculated I-131 concentrations between the two nuclear codes and differences in one-group constants calculated between the two nuclear libraries used in the evaluations (ENDF/B-VII.1 and JENDL-3.2). For their reactor, the VisualBurnOut code calculated one-group cross-sections of Te-130 of 0.085 barns and 0.06 barns using the JENDL-3.2 and ENDF/B-VII.1 nuclear libraries, respectively–a difference of about 30%. Coincidentally, the calculated I-131 concentrations also differed by about 30%, as would be expected. Kochnov also compared the results of I-131 concentrations between the VisualBurnOut and ORIGEN-S codes. In this comparison, VisualBurnOut utilized the JENDL-3.2 library to develop one-group constants whereas the ORIGEN-S code utilized the ROSFOND library. Similarly to the differences between the nuclear libraries, the ORIGEN-S and VisualBurnOut codes produced different final activities of I-131 of 252.0 and 191.4 Ci, respectively. The authors reasoned that the differences may be attributed to the resonance structure of tellurium and preparation of one-group constants by the two different codes. The authors believe the large resonance cross-section of Te-123 (5640 barns) is the main contributor to a flux dip across the target, which if underestimated, could produce an overestimation of the Te-130 neutron absorption cross-section. The authors believe that the ORIGEN-S code fell victim to this reasoning mainly because the 299-group spectrum used to calculate one-group constants in MCNP for the ORGIEN-S code was not sufficient to account for the self-shielding across the sample.

In addition to disputes in literature over the neutron absorption cross-sections, the actual calculations for I-131 yield and optimal cooling times to produce the maximum amount of I-131 activity post irradiation in literature are also inconsistent and frequently erroneous. Mostafa in [15] used a mathematical model to calculate the radioactive yields of Te-131 and Te-131m, A_0 (Bq), during irradiation according to the formula

$$A_0 = \frac{N_A}{M}\sigma\phi m(1 - \exp^{-\lambda_0 t}) \tag{1.6}$$

where N_A is Avogadro's number, M the molar mass of the target, σ the cross-section corresponding with the respective reaction, ϕ the neutron flux, λ_0 the respective nuclide's decay constant, m the target mass, and t the irradiation time. Mostafa calculated the final activity of the sample following irradiation according to the Bateman equation

$$N_n(t) = \sum_{i=1}^{n} \left[N_i(0) \times \left(\prod_{j=y}^{n-1} \lambda_j \right) \times \left(\sum_{j=i}^{n} \frac{(e^{-\lambda t})}{\prod_{p=i,p\neq j}^{n} (\lambda_p - \lambda_j)} \right) \right] \tag{1.7}$$

where n represents the number of nuclides in the chain, N the number of atoms, t the time following irradiation, and λ the decay constant. In the calculations, Mostafa utilized a Te-130 thermal cross-section of 0.20 + 0.04 barns, an isotopic abundance in natural tellurium of 33.8%, a 1 gram tellurium target, an irradiation time of 24 hours and a neutron flux of $1 \times 10^{13}\ n \cdot cm^{-2} \cdot s^{-1}$. The I-131 yield calculated during irradiation are reasonable and consistent with other results from literature and are shown in Table 1.3.

Table 1.3: Reported I-131 radioactivity during irradiation of a 1 g tellurium target in a thermal neutron flux of $1 \times 10^{13}\ n \cdot cm^{-2} \cdot s^{-1}$ in [15]

Irradiation Time (days)	Reported Activity (GBq)
1	0.315
7	1.732
60	3.804

However, the calculations for I-131 activity following irradiation (during cooling time) appear incorrect. The calculations in [15] determined that a maximum activity of 20.99 GBq occurs at approximately 90 hours post-irradiation. Two calculations–one for the number of I-131 atoms required to produce an activity of 20.99 GBq and a second to determine the total number of Te-130 atoms transmutated (absorbed a neutron) during irradiation–can show that an activity this large is impossible to acquire with the parameters stated in the paper.

The amount of I-131 required to produce this activity is about 2.0997×10^{16} atoms, calculated from the formula

$$N_{I131} = \frac{A_{I131}}{\lambda_{I131}} \tag{1.8}$$

where N_{I131} is the number of I-131 atoms, A_{I131} the activity of I-131 in Bq (decays per second), and λ_{I131} the decay constant of I-131 provided in Section A.1 Table A.1 of the Appendix. The formula to calculate the total number of Te-130 atoms transmutated during irradiation is

$$\#\text{ transmutated atoms} = N\sigma\phi t \tag{1.9}$$

where N is the number of Te-130 atoms calculated by multiplying the number of moles of natural tellurium in the target times the isotopic abundance of Te-130 and Avogadro's number, and t is the length of irradiation. Utilizing this formula and the aforementioned constants used in [15], only 2.645×10^{15} Te-130 atoms transmutated during the 24-hour irradiation. This is the total number of I-131 atoms that the irradiation would produce (integrated from time zero to infinity) since the decay chains that result from this reaction decay into I-131, yet 2.645×10^{15} atoms is still a factor of ten smaller than the instantaneous 2.0997×10^{16} I-131 atoms required to produce the stated activity of 20.99 GBq 90 hours after the completion of irradiation.

Additionally, the stated optimal cooling time of 90 hours to produce this maximum activity in [15] appears suspect. Mostafa reasonably calculated that the overall contribution of I-131 from both decay branches of Te-131m (refer to Equations 1.4 and 1.5) is small during irradiation compared to that of Te-131 (Equation 1.3). This is logical because the Te-130 cross-section used in [15] that yields Te-131 (0.2 barns) is five times larger than that which yields Te-131m (0.04 barns). Thus, Te-131 receives five times the number of atoms from the neutron capture of Te-130 over Te-131m. Additionally, the half-life of Te-131 is significantly shorter than that of Te-131m at 25 minutes compared to 33.25 hours, respectively. Therefore, Te-131 produces I-131 much quicker than Te-131m does due to this higher the specific activity. Since the neutron capture of Te-130 results in significantly more Te-131 than Te-131m and the half-life of Te-131 is shorter, it would be intuitively stunning if the activity of I-131 peaked after no more than a few half-lives of Te-131 were spent. The suggestion that the peak activity occurs at 90 hours–when Te-131 has been eradicated since approximately four hours post-EOI–appears erroneous.

Surprisingly, the stated optimal cooling time of 90 hours in [15] coincides with the optimal cooling time of 96 hours given by Alanis in [5]. The work in [5] discusses experiments performed as a precursor to industrial scale production of I-131 via the neutron irradiation of tellurium at a Triga Mark III reactor. These experiments determined the optimal heating conditions to produce cavities in crystalline TeO_2 where I-131 gases are absorbed. Following irradiation, the cylindrical TeO_2 was manipulated in a hot cell and melted to release the iodine gas, which was bubbled in two solutions before being filtered via activated carbon and alumina filters. The recovery yield of I-131 (percent of I-131 collected from the irradiated sample via processing) was not provided, but the collection efficiency of I-131 that was released in gaseous form was 99.9%, [5]. The discussion of the optimal irradiation and cooling times to produce the maximum amount of I-131 activity in [5] was brief.

The experiments in [5] utilized a 10 g sample of sintered TeO_2 in a neutron flux of 1.65×10^{12} n·cm^{-2}·s^{-1}. In that work, the optimal irradiation time was stated as 150 minutes based on the time to acquire saturation of Te-131. Although [15] agrees that 150 minutes is approximately the amount of time required to saturate Te-131 in the sample and Te-131 is the main contributor to I-131, this stated optimal irradiation time does not consider the influence of Te-131m contributing to the I-131 activity or the fact that the longer half-life of I-131 allows the activity from Te-131 to build up over time during irradiation. Thus, this stated optimal irradiation time appears over-simplified for the total process.

Similarly, the calculation for a "suitable" cooling time in the same paper ([5]) also appears to be oversimplified. This work references the Bateman equation shown in Equation 1.7 to calculate a minimum cooling time of 96 hours. It appears plausible that Alanis differentiated Equation 1.7 to solve for the optimal cooling time of the sample in [5] to the form of

$$t_{max} = \frac{1}{\lambda_2 - \lambda_1} \ln \frac{\lambda_2}{\lambda_1} \tag{1.10}$$

where t_{max} represents the optimal cooling time, λ_2 the decay constant of I-131, and λ_1 the decay constant of Te-131m, without considering the contribution from Te-131. Additionally, both [15] and [5] recognize that Te-131 is the main contributor of atoms to I-131, but the half-life of Te-131 is only 25.0 minutes. Based on this statement, it is again unclear why the

maximum activity of I-131 should occur when over two hundred half-lives of Te-131 have been consumed (the largest contributor of I-131 activity). Ultimately, [5] measured an I-131 activity of approximately 1.48×10^6 Bq/g Te from the irradiation of 10 g of tellurium for 2.5 hours with 96 hours of cooling time.

Alanis published another paper in [4] that again focused on experimental methods to produce I-131 via the neutron irradiation of Te-130. Those experiments produced TeO_2 by mixing tellurium with HNO_3 and sintering the solution. After irradiation, an oven heated the source to melting to release the I-131, the vapors bubbled through two solutions and finally passed through an activated carbon filter. Again, there was no recording of the recovery yield of I-131, but the process did collect 99.9% of the I-131 released from the TeO_2.

In [4], the optimal irradiation time remained the same as the other work in [5] at 2.5 hours because Alanis presumed that since Te-131 is the main contributor of activity to I-131 and Te-131 reaches saturation at 2.5 hours of irradiation time in the aforementioned thermal neutron flux of 1.65×10^{12} $n \cdot cm^{-2} \cdot s^{-1}$, there is no reason to continue irradiating the sample. This is again an oversimplified view of the process and does not consider the significantly longer half-life of I-131 and the activity of I-131 that grows over the duration of the irradiation. Alanis presented the cooling time in this work as a minimum of 3.7 hours, which is arrived at by utilizing Equation 1.10 but only including the half-lives of Te-131 and I-131 and disregarding Te-131m. This formula ignores the quantities of all the nuclides at the end of irradiation, which must be considered to accurately determine a suitable or optimal cooling time of the sample. This experiment finally yielded 3.145×10^8 Bq/g Te of I-131 following an irradiation of 24 hours and a 48 hour cooling time.

El-Absy published a work in [8] mainly focused on extracting I-131 from a tellurium dioxide target via the wet-distillation method. El-Absy irradiated 2 gram samples of tellurium dioxide wrapped in aluminum for four hours in a neutron flux of approximately 10^{14} $n \cdot cm^{-2} \cdot s^{-1}$at the ETRR-2 Research Reactor in Egypt. El-Absy reasoned that since the contribution of I-131 activity from Te-131 (Equation 1.3) is much greater than that from Te-131m (Equation 1.4) and Te-131 has a very short half-life of 25.0 minutes, a cooling period of less than two days was sufficient to allow satisfactory yields of I-131. Although intuitive, there was no mathematical justification for this cooling time in [8].

After the two day cooling period, the samples, their aluminum wrappers, and other additives were dissolved in sodium hydroxide and mixed with distilled water, sulphuric acid, and hydrogen peroxide. The actual distillation of iodine resulted from boiling the solution, passing the gaseous mixture through an acid filter and eventually through two alkali receivers that collected the iodine in the form of sodium iodide. This experiment showed this process to be efficient and collect 94.6% of the I-131 from the irradiated TeO_2 sample for a total of 3.382×10^8 Bq/g Te, [8].

Mohamed's thesis in [14] discusses a dry distillation method of separating I-131 from an irradiated TeO_2 target. Following irradiation, Mohamed placed the target in an oven and heated it to below melting temperature of the target, which released the I-131 in a gaseous state over a period of time that a sodium hydroxide solution captured. The I-131 yield following the irradiation of 5 g of natural TeO_2 in a neutron flux of 1×10^{14} $n \cdot cm^{-2} \cdot s^{-1}$at the ETRR-2 reactor produced 103 mCi or activity in the target, or 9.53×10^8 Bq/g Te. Mohamed varied a variety of the experimental parameters–including distillation time and temperature, amongst others–and summarized and stated optimum conditions for I-131 production and subsequent processing. These optimum conditions referred to an irradiation time of 12 hours and cooling time of 48 hours, which are more than likely experimental parameters used in the research, not optimum values since there is not a discussion of those calculations present in the research.

The lack of coherency in literature between the Te-130 cross-section, final yields of I-131, and optimal cooling time of the irradiated sample that produces the maximum amount of I-131 makes it difficult to predict the total amount of I-131 that would be produced by a nuclear reactor. The purpose of this work was to clarify these discrepancies utilizing an analytical model and experimental data.

Chapter 2

Methodology

This work utilized an analytical model constructed in Mathematica 11 ([Inc.]) to calculate I-131 yields resulting from the neutron irradiation of natural tellurium. The code consisted of three parts: a solution to the rate equations that represented the number of atoms of each nuclide in the system; a non-linear least-squares solver that fit variables in the solutions of the equations to experimental data; and lastly a Monte Carlo analysis that allowed either portion of the code to be run with many histories to determine the variances and covariances in the system.

In order to solve the differential equations and acquire a function of the number of atoms of each nuclide in the system, the equations were linearized via the Laplace transform and placed in matrix form. The linear matrix was solved by applying Gauss elimination to yield the solution of the rate equations in the complex domain. Instead of taking the inverse Laplace transform directly, the code applied Cauchy's residue theorem, which eliminated the complexities involved with evaluating the inverse Laplace transforms and reduced the calculation to a systematic process of factoring. canceling terms, and taking simple derivatives of polynomial functions. The end result was a symbolic solution to the rate equations that could be left as functions of any of the user's desired parameters. Any analysis in this work that only required a solution of the number of nuclides could be done with these equations. Further manipulation was not required.

However, in cases where the user needed to fit a parameter that was left as a symbolic variable in the solutions to the rate equations, the problem had to be solved as a linear regression problem. The Gauss-Newton algorithm was used for this purpose.

Lastly, a Monte Carlo addition was added in order to account for the variances and covariances in the system. The Monte Carlo analysis utilized a user defined library of uncertainties to draw random values from. The Monte Carlo analysis worked with both of the precursor parts of the code. The sections in this chapter discuss the methodology of the basis of each of these three parts.

2.1 Solution to the Rate Equations

The amount of a nuclide, f_i, at some time, t, can be calculated by integrating the equation

$$\frac{df_i}{dt} = \sum_{j=1}^{n} f_j(t)\Big(\sigma_j \phi_j \gamma_{j\to i} + \lambda_j P_{j\to i}\Big) + S_i(t) \tag{2.1}$$

where f_i is the number of atoms of the nuclide of interest, n the total number of nuclides considered in the evaluation, σ the neutron absorption cross-section in cm^2, ϕ the neutron flux in $n{\cdot}cm^{-2}{\cdot}s^{-1}$, $\gamma_{j\to i}$ the probability of a neutron absorption by isotope j resulting in isotope i (fractional yield from neutron absorption), λ the decay constant in s^{-1}, $P_{j\to i}$ the probability of the decay of isotope j resulting in isotope i (decay fractional yield), and $S_i(t)$ the external feed of nuclide i from external sources not considered in the analysis. The sum term from nuclide j to n in Equation 2.1 must also include the loss of isotope i due to its decay and neutron absorption. When the expression inside the sum evaluates the ith nuclide, the $\gamma_{j\to i}$ and $P_{j\to i}$ simply become -1, representing a loss of nuclide i.

The constants in this equation are not limited to scalars. The flux term could represent a continuous distribution integrated over the energy spectrum of neutrons in the reactor or a discrete set of values provided continuous or discrete cross-sections and γ-constants are similarly defined, respectively. The constants from Equation 2.1 used in this work are shown in the Appendix, which includes the λ, γ, and P constants.

There are notable differences between the derivation of the solution to Equation 2.1 in this work and advanced nuclear codes, specifically the program ORIGEN that is part of the SCALE software suite. ORIGEN is used to calculate compositions and radioactivity of fission products or the final result of an activation problem. ORIGEN is a mature and complex code that integrates a variety of data (ENDF, JEFF, etc.) into the solution of Equation 2.1. ORIGEN focuses on generating one-group cross-sections from multi-group fluxes and cross-sections. Additionally, ORIGEN considers all reaction types available in the database it exploits (i.e. (n, n), (n, 2n), (n, α), etc.) for each nuclide. The code averages all of these reactions for the f_j and σ_j terms and condenses the multi-group equation into a single group equation. ORIGEN's method of solving the one-group ordinary differential equation provided in Equation 2.1 is to use a series expansion of the matrix exponential solution. There are variety of shortcuts and alternative procedures that ORIGEN uses to perform the calculations in order to increase the accuracy and reduce the memory and time required to acquire the final solutions.

In general, a user of ORIGEN is interested the final result of a process when used for an activation case. The user has the ability to manually change cross-sections and other data with their own user defined library, but ORIGEN will ultimately solve for the amount of each nuclide at the end of the user defined series of events. Additionally, this complex code requires the user to provide a fuel model of a reactor (typically performed using TRITON) before it will perform activation calculations.

The code of this thesis solves the system of equations from Equation 2.1 utilizing an analytical approach with Mathematica ([Inc.])–a symbolic programming language. An advantage of the methodology of this work over other similar programs is the ability of the code to solve for various parameters and constants in Equation 2.1 based on empirical data acquired from experimentation. Many of the parameters in activation calculations in this work (i.e., the production of I-131 from the neutron irradiation of Te-130) are either unknowns or have high uncertainties. Thus, the code can calculate a functional approximation to some of these parameters with sufficient experimental data.

The solving capabilities in the code used in this work are possible due the the symbolic language of Mathematica and analytical solutions to the rate equations of the system.

The derivation of the analytical solutions utilize the Laplace transform to linearize the rate equations shown in Equation 2.1, which makes the equations significantly easier to manipulate and solve analytically. The Laplace transform is formally defined by

$$\mathscr{L}\{f(t)\} = F(s) = \int_0^\infty f(t)\mathrm{e}^{-st}\mathrm{d}t \tag{2.2}$$

for all $t \geq 0$, where $F(s)$ is the Laplace transform of $f(t)$ and s is a complex number given by

$$s = \sigma + j\omega \tag{2.3}$$

where σ and ω are real numbers and j is the imaginary unit. The Laplace transform of Equation 2.1 is

$$sF_i(s) - f_i(0) = \sum_{j=1}^{n} F_j(s)\Big(\sigma_j\phi_j\gamma_{j\to i} + \lambda_j P_{j\to i}\Big) \tag{2.4}$$

where $f_i(0)$ is the number of atoms of nuclide i at $t = 0$. Rearranging this linear expression in the complex domain yields a system of equations in the generic form of

$$[\mathbf{A}]\{\mathbf{x}\} = \{\mathbf{b}\} \tag{2.5}$$

, where the $\mathbf{A}$ coefficient matrix is an $n \times n$ matrix (n representing the number of nuclides in the system), $\mathbf{x}$ a scalar column vector of the number of each nuclides, and $\mathbf{b}$ the scalar column vector containing the initial amounts of each of the nuclides. After summarizing the constants with the notation

$$gain_{i,j} = \sigma_j\phi_j\gamma_{j\to i} + \lambda_j P_{j\to i} \tag{2.6}$$

where $gain_{i,j}$ denotes the gain in number of atoms per second of nuclide i from nuclide j, the system of equations given by Equation 2.4 is explicitly defined in the transformed domain

by

$$\begin{bmatrix} -s+gain_{1,1} & gain_{1,2} & \cdots & gain_{1,n} \\ gain_{2,1} & -s+gain_{2,2} & \cdots & gain_{2,n} \\ \vdots & \vdots & \ddots & \vdots \\ gain_{n,1} & gain_{n,2} & \cdots & -s+gain_{n,n} \end{bmatrix} \begin{Bmatrix} F_1(s) \\ F_2(s) \\ \vdots \\ F_n(s) \end{Bmatrix} = \begin{Bmatrix} f_1(0) \\ f_2(0) \\ \vdots \\ f_n(0) \end{Bmatrix} \tag{2.7}$$

The goal in the analysis was to solve this linear system of equations for the $F_1, F_2, \ldots, F_n$ array by employing Gaussian elimination. Gaussian elimination requires the formation of an $n \times n+1$ matrix, referred to as the augmented matrix, which takes the generalized form from Equation 2.5 of

$$[\mathbf{A}]|\{\mathbf{b}\} = \left[\begin{array}{cccc|c} a_{1,1} & a_{1,2} & \cdots & a_{1,n} & b_1 \\ a_{2,1} & a_{2,2} & \cdots & a_{2,n} & b_2 \\ \vdots & \vdots & \ddots & \vdots & \vdots \\ a_{n,1} & a_{n,2} & \cdots & a_{n,n} & b_n \end{array}\right] \tag{2.8}$$

where the a values correspond with the *gain* terms in Equation 2.7 and the b values correspond with the initial amounts of each nuclide. Forward elimination consists of eliminating the terms in the augmented matrix shown in Equation 2.8 to create an upper triangular form of the augmented matrix. This process starts by eliminating the x_1 terms from rows 2 through n according to elementary row operations given by the formula

$$a'_{i,*} = a_{i,*} - \frac{a_{i,1}}{a_{1,1}} a_{1,*} \tag{2.9}$$

, where $a_{i,*}$ represents row i in the matrix and the prime indicates the number of times a value has been modified. Next, the x_2 terms are eliminated from rows 3 through n utilizing a similar equation, but performing the calculation on the new elements of the matrix (i.e., the a'_i terms)

$$a''_{i,*} = a'_{i,*} - \frac{a'_{i,2}}{a'_{2,2}} a'_{2,*} \tag{2.10}$$

, and repeating this process for all the x variables through the n-equation

$$a^{n-1}_{n,*} = a^{n-2}_{n,*} - \frac{a^{n-2}_{n,n-1}}{a^{n-2}_{n,n}} a^{n-2}_{n,*} \tag{2.11}$$

to finally provide the fully normalized matrix

$$[\mathbf{A}]'|\{\mathbf{b}\}' = \left[\begin{array}{cccc|c} a_{1,1} & a_{1,2} & \cdots & a_{1,n} & b_1 \\ 0 & a'_{2,2} & \cdots & a'_{2,n} & b'_2 \\ \vdots & \vdots & \ddots & \vdots & \vdots \\ 0 & 0 & \cdots & a^{n-1}_{n,n} & b^{n-1}_n \end{array}\right] \tag{2.12}$$

Back substitution then solves the equations in reverse order starting with the n row, for which the equation is simplified to

$$x_n = \frac{b^{n-1}_n}{a^{n-1}_{n,n}} \tag{2.13}$$

The remaining rows can then be solved according to the general form of the equation

$$x_i = \frac{1}{a^p_{i,i}}\left(b^p_i - \sum_{j=i+1}^{n} a^p_{i,j}x_j\right) \tag{2.14}$$

, where p is equal to the prime count, $n-1-i$. Solving this equation results in a non-linear solution to the amount of each nuclide as a function of the complex variable s. The complexity of the equations is dependent on the variables used in the analysis. When applying Mathematica's symbolic language to replace constants in the system with variables in preparation for non-linear regression, the equations become greatly obfuscated, resulting in poorly constructed functions of variables in the complex domain that are impractical or impossible to solve by applying Mathematica's built in inverse Laplace transform directly.

The code in this thesis solves this issue by solving the contour integral generated by the Laplace transform and matrix operations in the complex plane by utilizing Cauchy's residue theorem. Referring back to the formal definition of the Laplace transform provided in Equation 2.2, the inverse Laplace transform takes the form of a contour integral

$$f(t) = \mathscr{L}^{-1}\{F(s)\} = \frac{1}{2\pi j}\int_{\sigma-j\infty}^{\sigma+j\infty} F(s)\mathrm{e}^{st}\mathrm{d}s = \frac{1}{2\pi j}\oint_C F(s)\mathrm{e}^{st}\mathrm{d}s \tag{2.15}$$

, where j is the imaginary unit. This contour integral can be evaluated as a Bromwich contour, which consists of two integrals: a portion of a circle, C_1, with radius R; and the vertical line, L_1, shown in Figure 2.1.

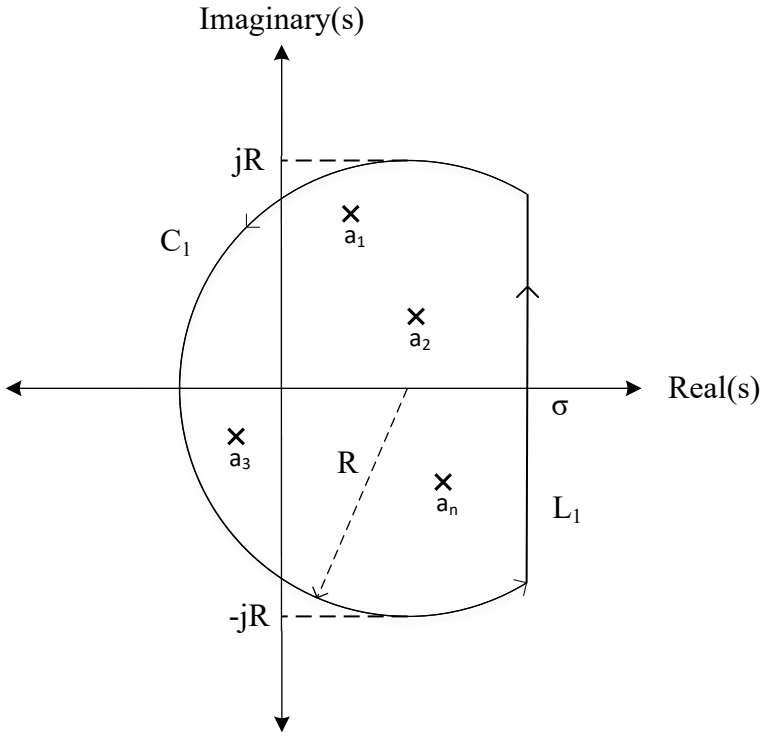

Figure 2.1: Bromwich contour whose integral consists of circular and line parts

Visually from Figure 2.1, the contour integral from Equation 2.15 can be divided into the C_1 and L_1 terms,

$$\frac{1}{2\pi j}\oint_C F(s)\mathrm{e}^{st}\mathrm{d}s = \frac{1}{2\pi j}\oint_{C1} F(s)\mathrm{e}^{st}\mathrm{d}s + \frac{1}{2\pi j}\oint_L F(s)\mathrm{e}^{st}\mathrm{d}s \tag{2.16}$$

Equation 2.16 is evaluated via Cauchy's residue theorem, which states that the line integral of a holomorphic function (differentiable in the complex plane in the neighborhood of all the points in its domain) around a closed contour γ that encompasses a fixed number of discrete points, $a_1, a_2, \ldots a_n$, is equal to $2\pi j$ times the sum of the residues of the function at

the discrete points. Cauchy's residue theorem can be expressed as

$$\frac{1}{2\pi j}\oint_{\gamma} f(z)\mathrm{d}z = \sum_{c=1}^{n} \mathrm{Res}[f(z), a_c] \tag{2.17}$$

, where n is equal to the total number of singular points, a, of $f(z)$. To clarify, $f(z)$ is not a function limited to the real domain. In fact, this function could very well be a complex function such as $F(s)$, as is used in this work, and is only meant as a generic representation of a function. As long as the line integral, L_1, from Figure 2.1 has a location to the right of all singular points n of $f(z)$ and the radius of the circle is chosen sufficiently large to encompass the points, this theorem can be used. Conveniently, the circular integral around region C_1 of Equation 2.16 approaches 0 as the radius of the circle approaches infinity, which is desirable to ensure the radius is large enough to encircle the singularities, n. The line integral around L from Equation 2.16 can then be evaluated at limits $\sigma \pm j\infty$, which simplifies and combines the expression from Equations 2.16 and 2.17 to

$$f(t) = \frac{1}{2\pi j}\oint_{\gamma} f(z)\mathrm{d}z = \frac{1}{2\pi j}\int_{\sigma-j\infty}^{\sigma+j\infty} F(s)\mathrm{e}^{st}\mathrm{d}s = \sum_{c=1}^{n} \mathrm{Res}[F(s)\mathrm{e}^{st}, a_c] \tag{2.18}$$

Residues are formally defined by Equation 2.17, but can also be defined simply as the coefficient of the z^{-1} term of a Laurent series expansion of $f(z)$, which devolves the residue equation into

$$\mathrm{Res}[f(z), a_c] = \frac{1}{(m-1)!}\lim_{z\to a_c}\left[\frac{\mathrm{d}^{m-1}}{\mathrm{d}z^{m-1}}((z-a_c)^m f(z))\right] \tag{2.19}$$

, where c is a pole of the function $f(z)$ of order m. To clarify the difference between the order of the pole, m, and the order of the polynomial or number of roots of the equation, n, consider two examples. For the first example, let $g(z) = (z-1)^{-1}$. The function on the denominator has an order of one ($n = 1$) at $z = 1$, which is a first order pole ($m = 1$). Second, if $h(z) = (z-1)^{-2}(z-2)^{-1}$, the polynomial in the denominator has an order of three ($n = 3$) with two poles: a double pole ($m = 2$) at $z = 1$ and a single pole ($m = 1$) at $z = 2$. Thus, the residue calculation provided in Equation 2.19 becomes a process of determining the singularities of the function of interest and the order of these poles.

In order to use this generalization of residues to solve the inverse Laplace transforms of the system of equations determined by Gaussian elimination via Equations 2.13 and 2.14, the equations need to be placed in a form that contains a single numerator and single denominator. That way the singularities easily surface as the roots of the polynomials of the single denominator of each equation. This can be done by evaluating each term of Equations 2.13 and 2.14 based on its operator (*Head* function in Mathematica) and forcing each term into a single numerator and denominator. Fortunately, due to the nature of the nuclide rate equations represented by the augmented matrix and the Gaussian elimination method of creating an upper triangular matrix, the denominators of each term are always irreducible polynomials. Therefore, the number of singularities and corresponding residues of each function given by Equation 2.13 is equal to the order of the s variable on the denominator. Additionally, the requirement to factor the denominators of the functions to determine order of the singularity, m, for use in Equation 2.19 is eliminated since the polynomials are irreducible–making all of the singularities simple poles with $m = 1$.

It is not possible to analytically compute roots of polynomials with orders greater than three (i.e., we do not have direct expressions for them) and higher-order polynomials surface regularly in the analysis aforementioned in this work. However, higher-order polynomials are solvable numerically and a generic expression of the product of roots can replace the polynomial. For a function that contains an n order polynomial of the variable z, this generic equation is given by

$$f(z^n) = \prod_{y=1}^{n} (z - \text{Root}[f(z^n), y]) \tag{2.20}$$

, where $\text{Root}[f(z^n), y]$ represents the y root of polynomial $f(z^n)$. As previously shown in Equation 2.18, $f(z)$ is equal to $F(s)\text{e}^{st}$ for an inverse Laplace transform. Additionally, if we define a solution to the rate equation given in Equation 2.14 in terms of numerator and denominator functions, $P(s)$ and $Q(s)$, the $F(s)$ part of the $f(z)$ equation in the complex domain evolves to

$$F(s) = \frac{P(s)}{Q(s)} \tag{2.21}$$

, and if we replace the denominator function according to Equation 2.20 it becomes

$$F(s) = \frac{P(s)}{\prod_{y=1}^{n}(s - \text{Root}[Q(s), y])} \tag{2.22}$$

where it is clear that the singularities of $F(s)$ are equal to the roots of the $Q(s)$ function, shown in Equation 2.22 as $\text{Root}[Q(s), y]$. Given that each of the n roots of the irreducible polynomial $Q(s)$ is unique and the roots are simple poles of the overall equation $f(z)$ ($m = 1$ as defined earlier), the residue at a discrete point $a_k = \text{Root}[Q(s), k]$ from Equation 2.19 becomes

$$\text{Res}[F(s)\mathrm{e}^{st}, a_k] = \lim_{s \to a_k} \left[(s - a_k])\frac{P(s)}{\prod_{y=1}^{n}(s - a_y)}\mathrm{e}^{st}\right] \tag{2.23}$$

, which then simplifies to

$$\text{Res}[F(s)\mathrm{e}^{st}, a_k] = \lim_{s \to a_k} \left[\frac{P(s)}{\prod_{\substack{y=1 \\ y \neq k}}^{n}(s - a_y)}\mathrm{e}^{st}\right] \tag{2.24}$$

To ensure Mathematica simplifies Equation 2.23 into Equation 2.24, the code actually utilizes a derivative in the denominator of the function with respect to the $(s - a_k)$ term, which yields the same result as Equation 2.24. Finally, the solutions to the inverse Laplace transforms and ultimately the system of equations of interest results from summing all of the n residues provided in Equation 2.18 according to the formula in Equation 2.23, which for the i nuclide in the system becomes

$$f_i(t) = \sum_{c=1}^{n} \text{Res}[F(s)\mathrm{e}^{st}, a_c] = \sum_{c=1}^{n} \left(\lim_{s \to a_c} \left[\frac{P(s)}{\prod_{\substack{y=1 \\ y \neq c}}^{n}(s - a_y)}\mathrm{e}^{st}\right]\right) \tag{2.25}$$

This equation is solved for each nuclide in the system and the $f(t)$ function represents the number of atoms of the respective nuclide at a time, t. Depending on the symbolic variables chosen for analysis, this equation may or may not be completely analytical in nature. Since it is not possible to analytically determine the roots of higher order polynomials, the equations are left literally with the Roots[f(z), y] terms in them until an evaluation is required. The code then numerically determines the roots of the polynomials, if necessary. The code used to evaluate Cauchy's residue theorem is shown in Appendix B.1.

2.2 Non-Linear Regression

The solutions to the number of atoms of each nuclide from the previous section could be left as functions of the user's specified parameters. In general, the equations were long and direct solutions to the variable-parameters did not exist. However, the parameters could be solved for using non-linear regression via the Gauss-Newton algorithm.

The Gauss-Newton algorithm is a numerical method that minimizes the squared residuals of non-linear models. This numerical approach relies on iterative calculations based on step changes in the variables of interest. Since this method minimizes the squared residuals of the functions, the system of equations must be entered into the solvable matrix as equal to zero (i.e., the equations must be the residuals). Since the solutions to the equations $f_i(t)$ shown in Equation 2.25 represent the number of atoms of the ith nuclide, the equations shown in Equation 2.25 must have the number of atoms of the respective nuclide subtracted from them in order for to get the full equation into residual form for the Gauss-Newton method,

$$r_k(\beta_1, \beta_2, \ldots, \beta_n) = \sum_{c=1}^{n} \text{Res}[F(s)\mathrm{e}^{st}, a_c] - f_k(t) \tag{2.26}$$

, where $r_k(\beta_1, \beta_2, \ldots, \beta_n)$ is the kth equation's residual that is a function of the n number of variables in the system, $\beta_1, \beta_2, \ldots, \beta_n$.

The iterative solution to the kth equation via the Gauss-Newton method in a system of n variables and m equations is given by a first-order Taylor series expansion

$$\begin{aligned} &\frac{\partial r_k^{(s)}}{\partial \beta_1}\beta_1^{(s+1)} + \frac{\partial r_k^{(s)}}{\partial \beta_2}\beta_2^{(s+1)} + \cdots + \frac{\partial r_k^{(s)}}{\partial \beta_n}\beta_n^{(s+1)} = \\ &-\beta_k^{(s)} + \frac{\partial r_k^{(s)}}{\partial \beta_1}\beta_1^{(s)} + \frac{\partial r_k^{(s)}}{\partial \beta_2}\beta_2^{(s)} + \cdots + \frac{\partial r_k^{(s)}}{\partial \beta_n}\beta_n^{(s)} \end{aligned} \tag{2.27}$$

provided by [7], where $\beta^{(s)}$ is the previous iteration's solution (or the initial guess supplied by the user) and $\beta^{(s+1)}$ is the new solution to be tried by the next iteration. The Gauss-Newton method requires the number of functions, m, to be greater than or equal to the number of variables, n.

After rearranging the kth residual equation shown in Equation 2.27 to solve for the β^{s+1} terms, the equation in matrix notation becomes

$$\{\boldsymbol{\beta}^{(s+1)}\} = \{\boldsymbol{\beta}^{(s)}\} - ([\mathbf{J}_r]^\intercal[\mathbf{J}_r])^{-1}[\mathbf{J}_r]^\intercal\{\mathbf{r}^{(s)}\} \tag{2.28}$$

, where $\mathbf{r}^{(s)}$ is a column vector of the residual equations of the s iteration that are functions of the variables chosen for analysis, $\beta_1, \beta_2, \ldots, \beta_n$, which comprise the column vector $\{\boldsymbol{\beta}\}$. The $\{\boldsymbol{\beta}^{(s+1)}\}$ and $\{\boldsymbol{\beta}^{(s)}\}$ terms represent column vectors of the $s+1$ and s iterations' solution to the variables, respectively. The Jacobian matrix, $[\mathbf{J}]$, is an $m \times n$ (number of equations $\times$ number of variables) matrix of partial derivatives of the functions, formally defined by

$$[\mathbf{J}] = \begin{bmatrix} \frac{\partial r_1^{(s)}}{\partial \beta_1} & \frac{\partial \beta_1^{(s)}}{\partial \beta_2} & \cdots & \frac{\partial r_1^{(s)}}{\partial \beta_n} \\ \frac{\partial r_2^{(s)}}{\partial \beta_1} & \frac{\partial r_2^{(s)}}{\partial \beta_2} & \cdots & \frac{\partial r_2^{(s)}}{\partial \beta_n} \\ \vdots & \vdots & \ddots & \vdots \\ \frac{\partial r_m^{(s)}}{\partial \beta_1} & \frac{\partial r_m^{(s)}}{\partial \beta_2} & \cdots & \frac{\partial r_m^{(s)}}{\partial \beta_n} \end{bmatrix} \tag{2.29}$$

, while the $([\mathbf{J}_r]^\intercal[\mathbf{J}_r])^{-1}[\mathbf{J}_r]^\intercal$ term represents the pseudoinverse of the Jacobian matrix provided $m \neq n$. In the case where the number of equations equals the number of unknowns, the method simplifies to

$$\{\boldsymbol{\beta}^{(s+1)}\} = \{\boldsymbol{\beta}^{(s)}\} - [\mathbf{J}_r]^{-1}\{\mathbf{r}^{(s)}\} \tag{2.30}$$

, which is the equation for Newton's method. The code evaluates Equation 2.28 multiple times until the maximum percent difference between the i and $i+1$ iteration is below a user-defined error limit, typically 10^{-5} for this work.

2.3 Monte Carlo Analysis

A simple way to evaluate the influence of discrete parameters on other variables in a system of equations is to evaluate the equations numerous times as functions of random variates of the system parameter's uncertainties via a Monte Carlo analysis. This work used a Monte Carlo analysis to evaluate all the parameters with uncertainties reported in literature or through experimentation at MURR (Missouri University Research Reactor). Some variables

were left as constants, namely the zero probabilities of nuclides transmutating into other nuclides (fractional yields) via decay or neutron capture. For example, it is impossible for I-131 to transmute into Te-130 after absorbing a neutron or beta decaying. Table A.1 of Appendix A displays the parameters used in the analysis with their uncertainties.

The user needed to define all the variables that should change with each iteration and input the distribution type and standard deviation of these variables into a user defined library. Mathematica generated the random variates defined by the user and applied them to the solutions to the equations at each iteration in the analysis. Depending on the user's requirement for a calculation, either the direct solutions to the number of atoms of the nuclides or the non-linear regression portions of the code defined in Sections 2.1 and 2.2, respectively, could use the Monte Carlo analysis.

2.4 Functionality and Challenges

The code allowed the user to chain systems of equations together for series of irradiations and cooling times. While many of the system parameters remained constant (i.e. decay constants, cross-sections), other variables such as the flux and time of each event varied between events in the series. The code handled a chained series of equations by replacing the initial amount of each nuclide for the current event with that of the previous event. For example, if the series of events of interest consists of a single irradiation of a target (event 1) followed by a cooling time before measuring the activity in the sample (event 2), and four nuclides are chosen by the user to follow (n=4), there will be four equations in the two different systems for a total of eight equations. The initial amount of the kth nuclide for the cooling event, $N_{k,2}(0)$, will be equal to the number of atoms following the irradiation event, $N_{k,1}(t_1)$. Similarly, any systems with series longer than two events all replace the $N_k(0)$ term with the previous event's $N_{k-1}(t_{k-1})$ term. Since ultimately the expressions for the $N_k(t_k)$ expressions have been solved for, anytime the $N_k(t_k)$ term appears the code also replaces it with the direct expression.

Although the time and memory consumption to apply this methodology is minimal when solving for the $N_k(t_k)$ expressions of the amount of the nuclides for many events chained

together in a series using the formulas derived in Section 2.1, the time and memory demand increased exponentially when the user performed a non-linear regression and subsequent Monte Carlo analysis to access the solving capabilities within the code. This is due to the replacement of the $N_k(t_k)$ expressions by the inverse Laplace transforms of previous events and leaving the functions in terms of user specified variables. The equations get significantly larger for each successive event. In fact, the equations can easily become functions of hundreds of thousands of terms. This is necessary, however, because without the replacement of the terms there would additional unknowns added to the equations and the system would become unsolvable. Additionally, since the Gauss-Newton method requires the partial differentiation of the expressions and the functions were not linear, the chained equations couldn't be evaluated sequentially by event. Figure 2.2 shows the exponential increase of memory used by the equations as the number of chained equations increased.

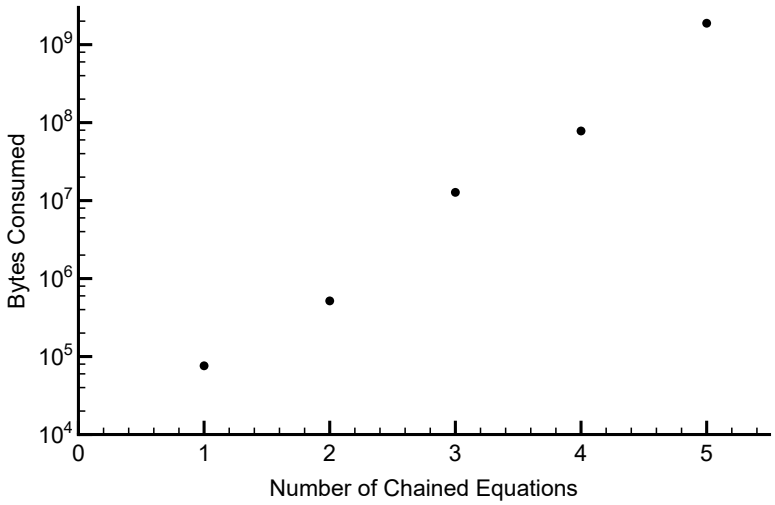

Figure 2.2: Memory usage as a function of the number of chained equations.

While this is a shortcoming of an analytical model, the advantage of the analytical solution was that the variables in the expressions could easily be changed to become continuous functions of other variables. This allowed for easy manipulation of the expressions and the ability to quickly determine dependence of variables on other parameters. Additionally, the code saved the random variates generated by the Monte Carlo analysis as well as the solutions to the variables of interest. After importing the saved data, the code

could easily reconfigure continuous expressions to replicate the same equations derived from the Monte Carlo analysis.

Another issue with the model is the lack of information supplied empirically for the calculations. In advanced nuclear codes such as MCNP or ORIGEN, the user can supply neutron flux energy distributions that the codes can use to calculate average cross-sections across the spectrum. While the code used in this work has the same functionality, the exact neutron flux energy distribution in the reactor or the cross-sections for the nuclides at the different energies is not empirically known. This is obviously problematic when the solving capabilities in the code are based off of empirical data inputs. However, the user is capable of inputing any number of energy groups as long as the corresponding cross-sections and fractional yields are also defined. In this sense, this code has the same functionality as MCNP or ORIGEN, but since the objective of the calculations is to generate the model off of empirical data, it is very difficult to do this precisely without knowing all the information exactly.

Chapter 3

Results

The discrepancies in literature over the the nuclide cross-sections, fractional yields of Te-131 and Te-131m following a Te-130 (n, γ) reaction, optimal cooling time, self-adsorption of the natural tellurium target, and yield of I-131 pose significant challenges in designing the process to produce I-131. The analytical model for the present calculations was configured with experimental data from MURR to acquire distributions for system parameters (cross-sections and fractional yields) and validate the model. After confirming the accuracy of the model's calculations, the model was rearranged to determine the optimal cooling time of the TeO_2 target that results in the largest I-131 activity and the yields of the nuclides as a function of the irradiation time.

MURR provided four sets of experimental data with different irradiation times and sample masses initially, then provided five additional runs that were trials for the actual target size and process that MURR will use to commercially produce I-131. The calculations of this work utilized mainly three of the first four data sets, which Table 3.1 summarizes. MURR measured the thermal neutron fluxes by irradiating in the same position as the samples two neutron density monitors (dilute Au-in-Al; RE-602C-Lot1; 0.01403 g; 1331.6 ppm Au and dilute Co-in-Al; NIST SRM 953; 0.01341g; 1160 ppm Co) that were vacuum-heat-sealed in a single quartz vial. Although the flux measurement was capable of measuring both a thermal and epithermal flux, only the thermal flux was considered for this work. The effects of the epithermal and fast flux were not considered. The goal of the model's calculations was to construct a functional estimate of unknowns in the system for MURR's

I-131 production. Generalizations were made for some of the calculations to accommodate I-131 generation at other reactors and their various system parameters. The uncertainty in the flux measurements for all of the experiments was ±5%. Refer to Appendix A for detailed descriptions of uncertainties used in the Monte Carlo analysis for the experiments.

Table 3.1: Summary of experiments used in this work provided by MURR

Experiment Number	Natural Tellurium Sample Mass	Irradiation Time	Neutron Flux	I-131 Yield
1	170.7 g	0.5 hours	9.9×10^{13} n·cm^{-2}·s^{-1}	0.879 ± 0.019 mCi/g TeO_2
2	0.1231 g	10 seconds	6.5×10^{13} n·cm^{-2}·s^{-1}	Various
3	1.0×10^{-4} g	150 hours	9.78×10^{13} n·cm^{-2}·s^{-1}	Various

The following items were analyzed sequentially to help resolve discrepancies in literature to help predict final yields of I-131 more accurately in this work:

1. Eliminated some of the unknowns in the system by determining that the (n, tot) cross-sections of Te-131, Te-131m, and I-131 do not significantly impact the final yield of I-131 outside the error limitations of the model.

2. Used experimental data from MURR's Experiment 2 to generate distributions and means for the fractional yields of Te-131 and Te-131m ($\gamma_{Te130 \rightarrow Te131}$ and $\gamma_{Te130 \rightarrow Te131m}$, respectively) resulting from the Te-130 (n, γ) reaction (Equations 1.1 and 1.2, respectively) from a Monte Carlo analysis performed by the model. The model also determined the best-fit Te-130 (n, γ) cross-section. This experiment contained radiation measurements for Te-131, Te-131m, and I-131.

3. Performed the same analysis as discussed in item 2 but for MURR's Experiment 3, which included data only for the yield of I-131 at various cooling times.

4. Generated a Te-130 (n, γ) cross-section distribution based on experimental data for a larger sample mass of natural tellurium (170.7 g). Only a single radiation measurement was taken of I-131 for this experiment.

5. Calculated optimal cooling times of the natural tellurium sample before processing to obtain the maximum I-131 yield for a variety of experimental conditions.

6. Calculated the estimated yield of Te-131, Te-131m, and I-131 for various experimental parameters using the calculated cross-sections and fractional yields from the previous analyses.

It is important to note that while the code was able to solve for the neutron absorption cross-section of Te-130 based on the yield of I-131, MURR did not measure the activities of other nuclides that could result from the neutron absorption of I-131, Te-131, or Te-131m and the data was therefore not available. Thus, any reference to the neutron absorption cross-section of these three nuclides in this work refers to the (n, tot) thermal reaction since the radiation measurement data of successive nuclides was not available to discriminate between specific reactions.

3.1 Elimination of Insignificant Parameters

As discussed in Section 2.3, the number of parameters the Gauss-Newton method can perform a least-squares fit of residuals to is limited by the number of equations supplied to the function. There are various parameters in the I-131 production process that have been studied very little or are highly disputed in literature, such as the cross-sections of Te-130, Te-131, Te-131m, and I-131 as well as the fractional yields of Te-131 and Te-131m from the Te-130 (n, γ) reaction. Since there was limited radiation data available and some of these unknowns do not contribute at all to the final yields of the nuclides, it was impossible for the code to find best-fits for all of the parameters at once. Thus, the first step in the analysis process was to eliminate the unknown parameters from the Gauss-Newton method that do not significantly impact the end result.

This work utilized quantitative and qualitative methods to determine the importance of these unknown variables on the end product of I-131 via the computation of the covariance matrix, a comparison between the calculated number of atoms as a function of various cross-sections, and visual inspection of the resulting graphs. This work began the visual determination of the importance of the aforementioned unknown variables by analyzing the impact of the cross-sections of all the nuclides and comparing the calculated results with experimental results from MURR's Experiment 3. The details of this experiment and the uncertainties are shown in Appendix Section A.4. Thus, the analytical model used the predefined conditions from Experiment 3 and left the cross-sections as variables in order to determine graphically the impact of changes in the cross-sections on the yield of I-131. The following graphs may not be completely realistic in terms of I-131 yield since there are other assumptions and unknowns that have yet to be determined (namely, the self-absorption of the tellurium target and the fractional yields of Te-131 and Te-131m from the Te-130 (n,γ) reaction). This portion of the analysis ignored self-shielding effects and used published values from literature to determine the other constants in the system (refer to the Appendix Section A).

First, the I-131 (n, tot) cross-section was varied and the impact on the I-131 yield was examined. Figure 3.1 shows the result from this analysis and has the actual yield of I-131 ($5.5 \times 10^{15} \pm 0.1 \times 10^{15}$ atoms) from the experiment shown between the dashed lines (shaded gray area). The results showed that as long as the I-131 cross-section does not exceed approximately 1×10^{-18}, the impact of the cross-section on the final yield of I-131 is within the error of the model. Additionally, the cross-section is probably less than 1×10^{-18} since the experimental data falls in that range. Since the impact of the I-131 (n,tot) cross-section was insignificant and within the error of the calculation, the remainder of the analysis used the calculated cross-section from the ENDF database in [1].

Similarly, the model analyzed the cross-sections of Te-131 and Te-131m and the results are shown in Figures 3.2 and 3.3, respectively. The gray shaded area in between the dashed lines represents the actual yield of I-131 from the experimental data. Similarly to I-131, the cross-section of Te-131 did not make a significant difference outside the error of the model until the cross-section approached 1×10^{-18}. The Te-131m cross-section, however, did not

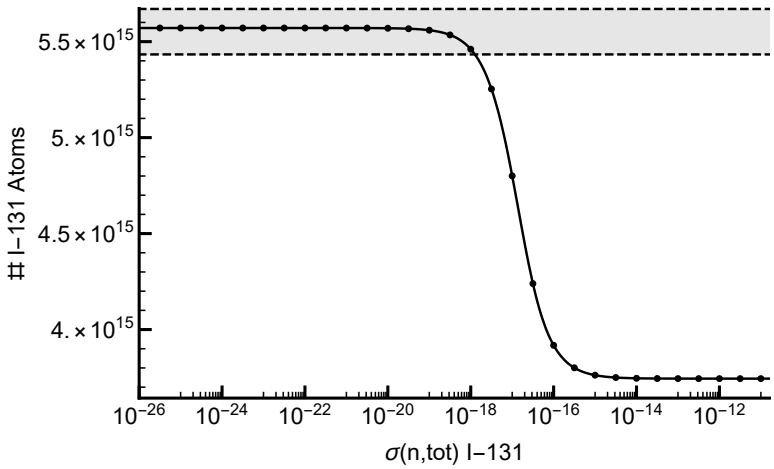

Figure 3.1: Yield of I-131 atoms as a function of the (n,tot) cross-section of I-131.

appear to impact the final yield of I-131 at all. Based on the small change in scale of the y-axis of this graph, the impact of Te-131m was deemed insignificant for the remainder of this analysis. This is mainly due to the low fractional yield of Te-131m from the Te-130 (n, γ) reaction (5%). Again, this is not a known or defined value exactly, only a placeholder for this portion of the analysis derived from nuclear libraries. Additionally, the longer half-life of Te-131m also reduced its significance in the total contributions of atoms to I-131 when compared to Te-131, as will be discussed later. The remainder of the analysis used the calculated cross-sections of Te-131 and Te-131m from the ENDF database in [1].

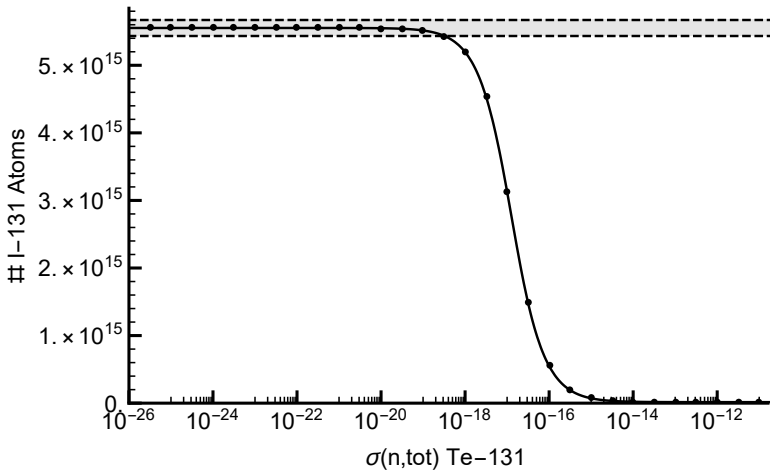

Figure 3.2: Yield of I-131 atoms as a function of the (n,tot) cross-section of Te-131.

Lastly, the code analyzed the impact of the Te-130 (n, γ) cross-section. Figure 3.4 shows the results. This reaction drives the entire process that the model analyzed and thus it

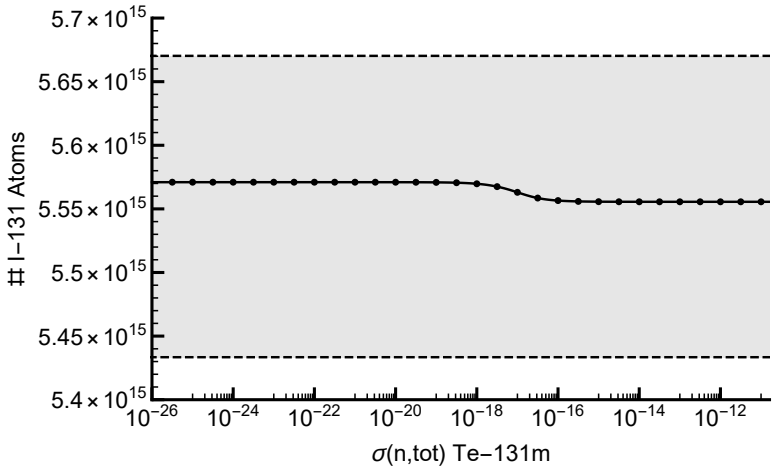

Figure 3.3: Yield of I-131 atoms as a function of the (n,tot) cross-section of Te-131m.

had a significant impact on the final yield of I-131. The actual yield of I-131 from the experiment is shown by the dashed line (since the scale changed so significantly as shown by the logarithmic y-axis, the uncertainty shaded area is not visually present). The function of I-131 atoms flattened at approximately 1×10^{-17} because at that high of a cross-section, all of the Te-130 atoms absorbed a neutron and were eliminated during irradiation.

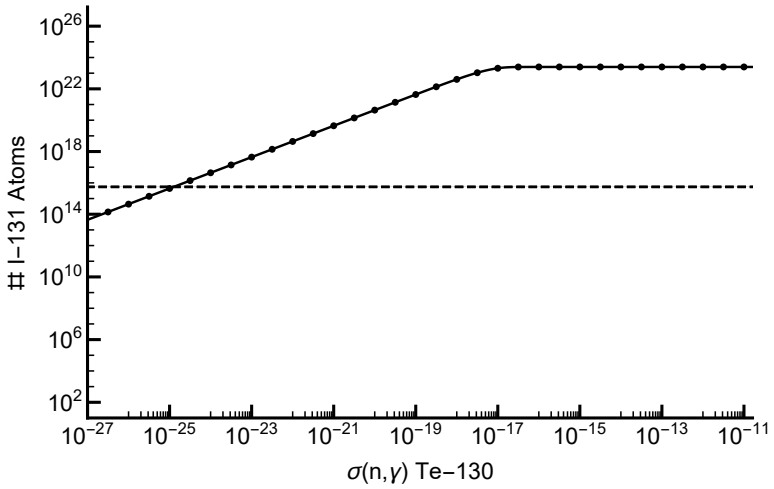

Figure 3.4: Yield of I-131 atoms as a function of the (n,γ) cross-section of Te-130.

Since the (n,tot) cross-sections of Te-131, Te-131m, and I-131 are within the error of the calculations and are insignificant to the final yield of I-131, the code is unable to solve for these unknowns. To further illustrate the lack of importance of these cross-sections over a variety of experimental conditions and not just those presented by Experiment 3 of this

work, the model calculated the final yield of I-131 atoms at the end of irradiation as a

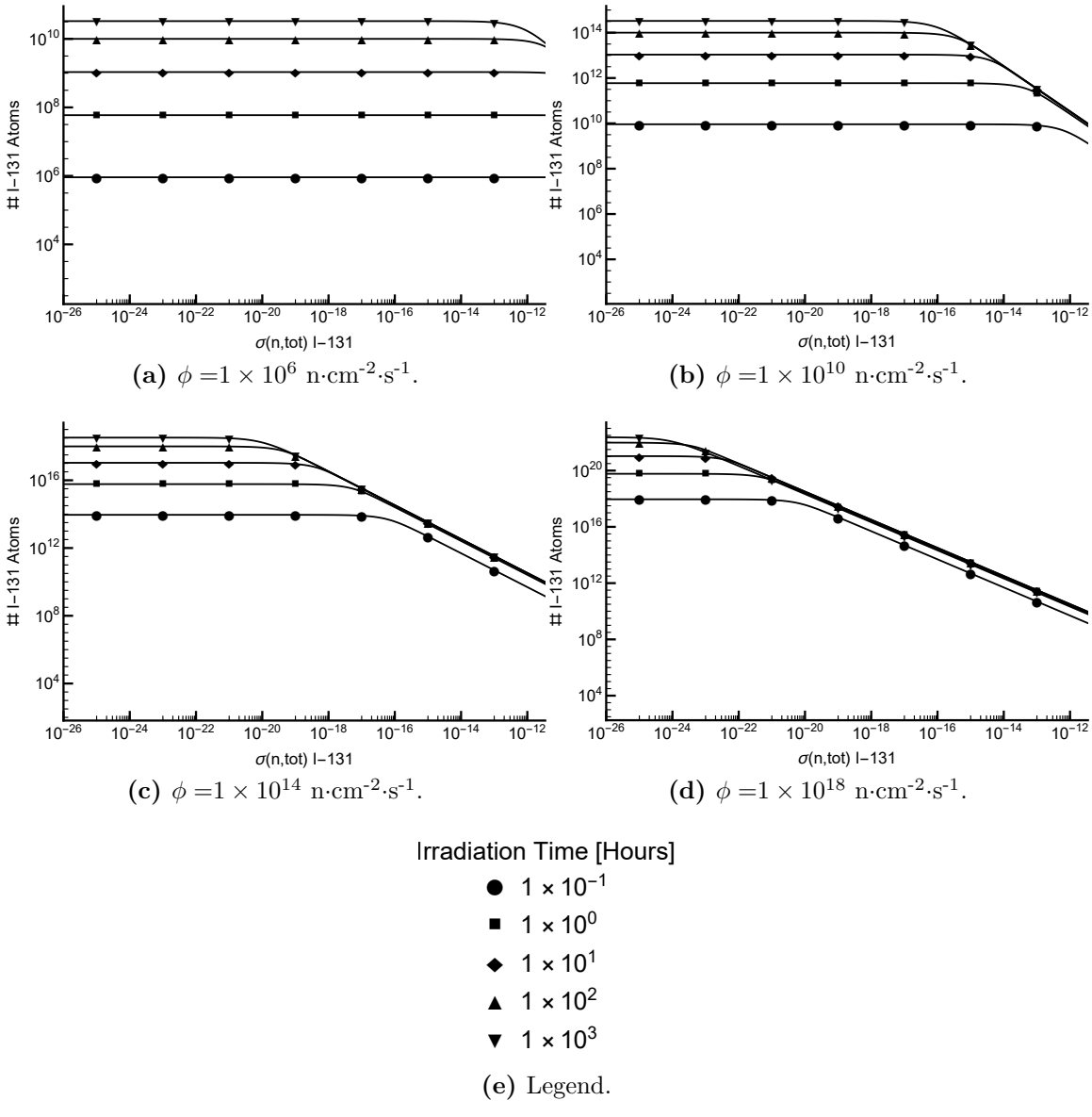

(a) $\phi = 1 \times 10^{6}$ n·cm^{-2}·s^{-1}.

(b) $\phi = 1 \times 10^{10}$ n·cm^{-2}·s^{-1}.

(c) $\phi = 1 \times 10^{14}$ n·cm^{-2}·s^{-1}.

(d) $\phi = 1 \times 10^{18}$ n·cm^{-2}·s^{-1}.

(e) Legend.

Figure 3.5: I-131 yield at end of irradiation as a function of the (n, tot) I-131 cross-section.

function of the cross-sections of each of I-131, Te-131, and Te-131m in Figures 3.5, 3.6, and 3.7, respectively, over various irradiation times and neutron fluxes for a 170.7 gram natural tellurium sample. In addition to these graphs, the same calculations for the Te-130 (n,γ) cross-section are shown in Figure 3.8. In the subplots for this data, the final yield of I-131 decreased at higher neutron fluxes and Te-130 (n, γ) cross-sections due to the total number of Te-130 atoms in the natural tellurium sample being transmutated earlier in the irradiation.

The earlier the atoms are transmutated, the longer time the I-131 atoms have to decay before the end of irradiation is reached. Thus, the final yield of I-131 decreased for these data sets. This effect would be lessened for larger sample masses of natural tellurium.

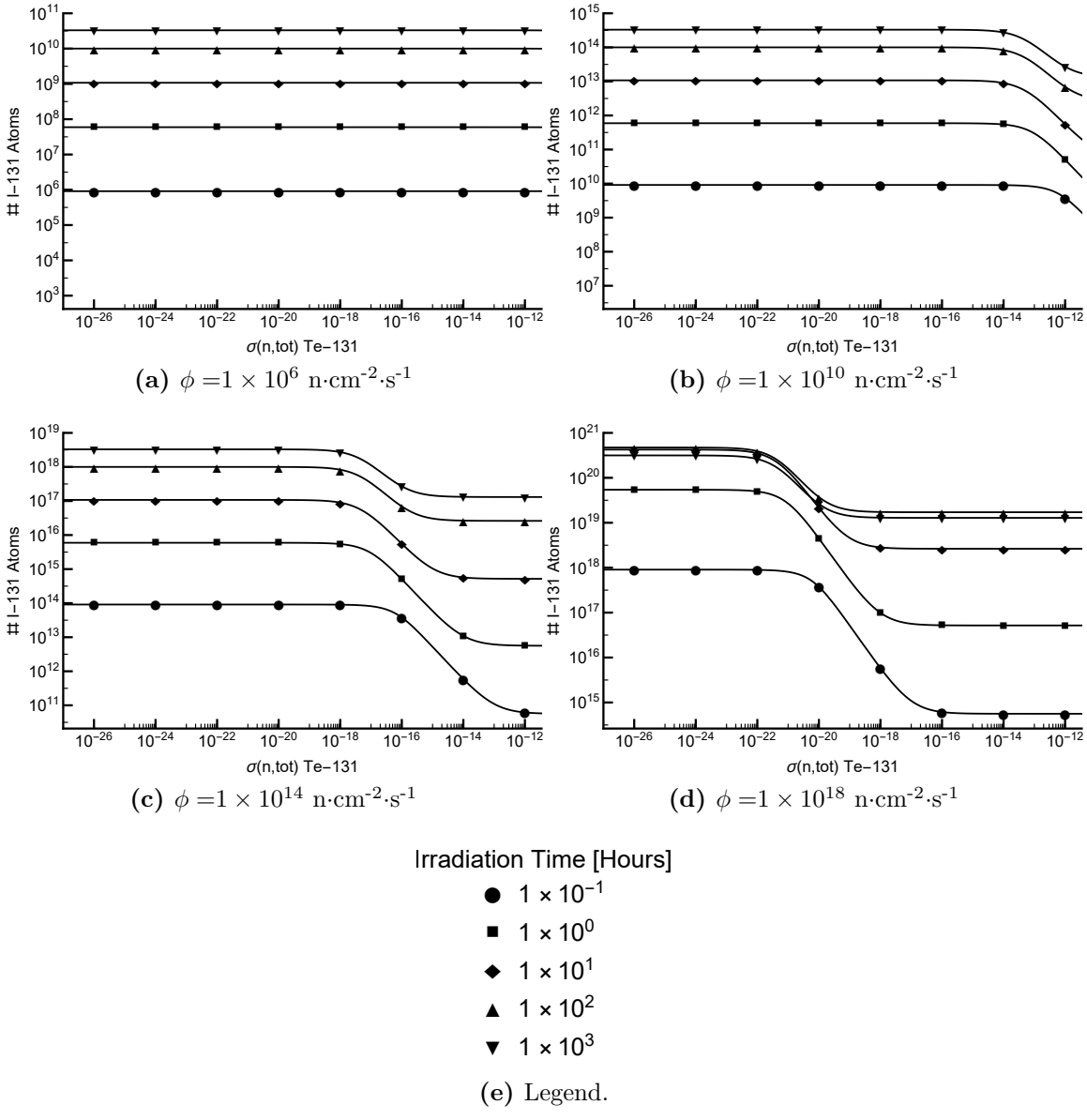

(a) ϕ =1 × 10^{6} n·cm^{-2}·s^{-1}

(b) ϕ =1 × 10^{10} n·cm^{-2}·s^{-1}

(c) ϕ =1 × 10^{14} n·cm^{-2}·s^{-1}

(d) ϕ =1 × 10^{18} n·cm^{-2}·s^{-1}

(e) Legend.

Figure 3.6: I-131 yield at end of irradiation as a function of the (n, tot) Te-131 cross-section.

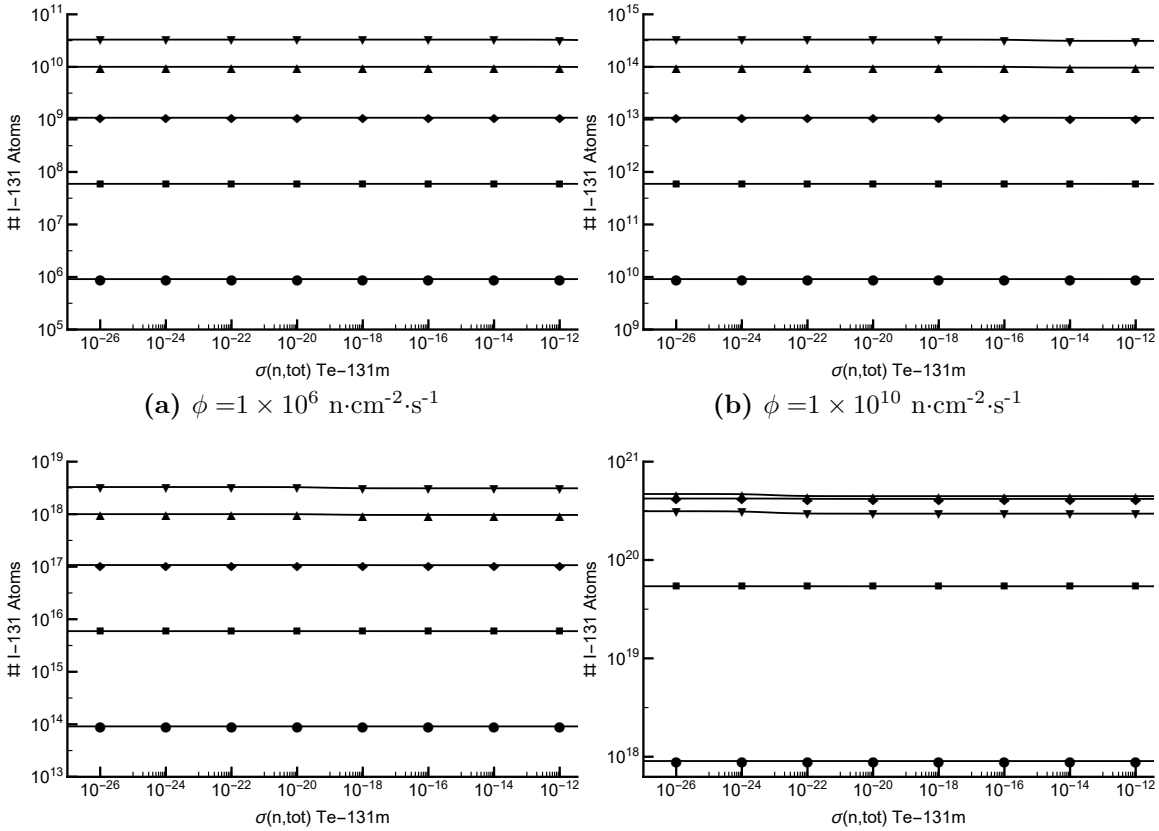

(a) $\phi = 1 \times 10^{6}$ n·cm^{-2}·s^{-1}

(b) $\phi = 1 \times 10^{10}$ n·cm^{-2}·s^{-1}

(c) $\phi = 1 \times 10^{14}$ n·cm^{-2}·s^{-1}

(d) $\phi = 1 \times 10^{18}$ n·cm^{-2}·s^{-1}

(e) Legend.

Figure 3.7: I-131 yield at end of irradiation as a function of the (n, tot) Te-131m cross-section.

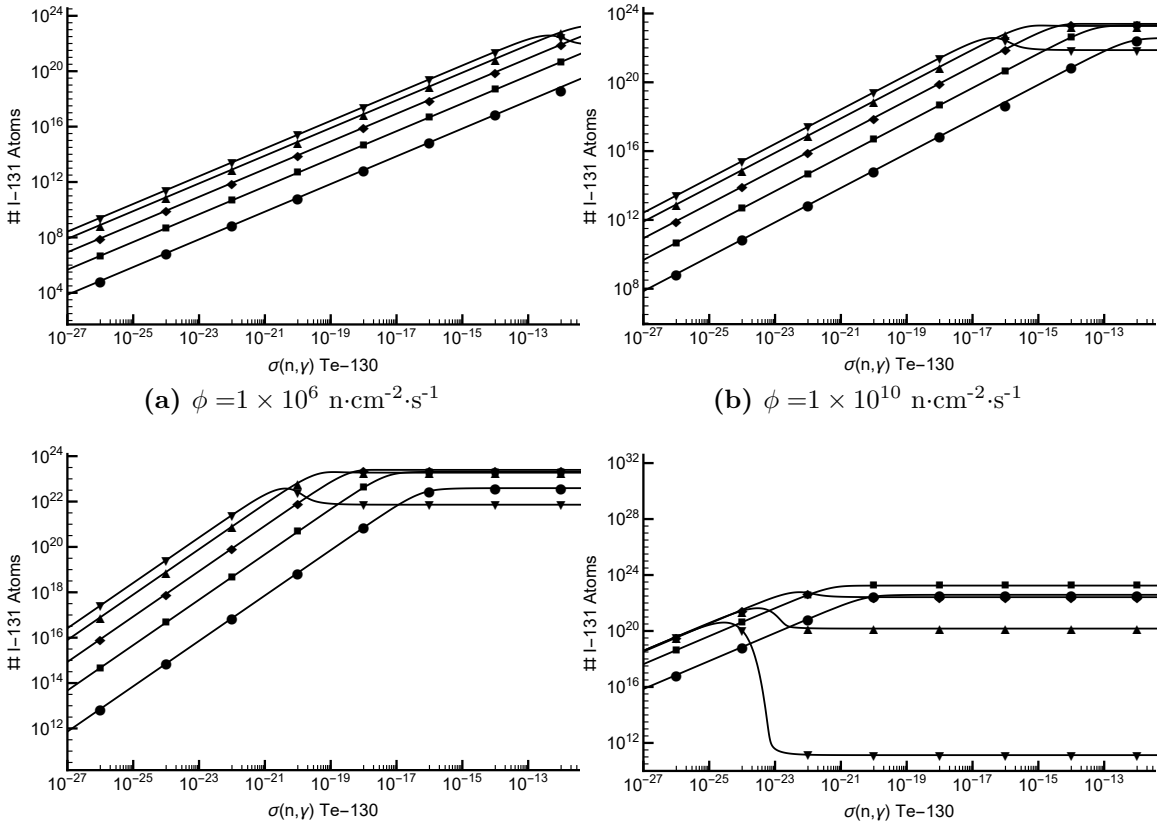

(a) $\phi = 1 \times 10^{6}$ n·cm^{-2}·s^{-1}

(b) $\phi = 1 \times 10^{10}$ n·cm^{-2}·s^{-1}

(c) $\phi = 1 \times 10^{14}$ n·cm^{-2}·s^{-1}

(d) $\phi = 1 \times 10^{18}$ n·cm^{-2}·s^{-1}

Irradiation Time [Hours]

- 1×10^{-1}
- 1×10^{0}
- 1×10^{1}
- 1×10^{2}
- 1×10^{3}

(e) Legend.

Figure 3.8: I-131 yield at end of irradiation as a function of the (n, γ) Te-130 cross-section.

3.2 Cross-Section and Fractional Yield Calculations

3.2.1 Experiment 2

The next part of the analysis utilized the results from MURR's second experiment to determine the fractional yields of Te-131 and Te-131m from the Te-130 (n, γ) reaction ($\gamma_{Te130\rightarrow Te131}$ and $\gamma_{Te130\rightarrow Te131m}$, respectively) as well as the Te-130 (n, γ) cross-section ($\sigma_{Te130}(n,\gamma)$). The second experiment from MURR was the only dataset available in this work that contained radiation measurements for Te-131 and Te-131m in addition to those for I-131.

This calculation required extra manipulation in the code. Due to the nature of the system and the experimental radiation measurements provided, it was not possible to separate the fractional yield terms from the Te-130 cross-section and acquire independent best-fits for both of the parameters at once. If the radiation from other nuclides had been measured, this more than likely would have been possible. Fortunately, due to the symbolic capabilities of the Mathematica code, the $\sigma_{Te130}(n,\gamma) \times \gamma_{Te130\rightarrow Te131}$ products (i.e., Te-130 (n γ) cross-section times the fractional yield of Te-131) were combined into a single term, $\sigma\gamma_{Te130\rightarrow Te131}$. Similarly, the $\sigma_{Te130}(n,\gamma) \times \gamma_{Te130\rightarrow Te131m}$ products were also combined into a single variable, $\sigma\gamma_{Te130\rightarrow Te131m}$. Even though there were only two variables, the three unknowns of interest (Te-130 cross-section and fractional yields of Te-131 and Te-131m) were still solved for according to the equations

$$\sigma_{Te130}(n,\gamma) = \sigma\gamma_{Te130\rightarrow Te131} + \sigma\gamma_{Te130\rightarrow Te131m} \tag{3.1}$$

$$\gamma_{Te130\rightarrow Te131} = \frac{\sigma\gamma_{Te130\rightarrow Te131}}{\sigma\gamma_{Te130\rightarrow Te131} + \sigma\gamma_{Te130\rightarrow Te131m}} \tag{3.2}$$

$$\gamma_{Te130\rightarrow Te131m} = \frac{\sigma\gamma_{Te130\rightarrow Te131m}}{\sigma\gamma_{Te130\rightarrow Te131} + \sigma\gamma_{Te130\rightarrow Te131m}} \tag{3.3}$$

$$1 = \gamma_{Te130\rightarrow Te131m} + \gamma_{Te130\rightarrow Te131} \tag{3.4}$$

The code applied the Gauss-Newton method to calculate the least squares fit of the $\sigma\gamma$ variables according to the non-linear model. Additionally, the analytical solution for the code was also computed with literature cross-sections to show the model's ability to

fit the parameters with the Gauss-Newton method. The comparison between the model's calculated best-fit Te-130 (n,γ) cross-section via the the method of least squares, the model's analytical calculation that utilized cross-sections from literature (non-iterative analytical), and the experimental results from MURR are shown in Figures 3.9a, 3.10a, and 3.11a for Te-131, Te-131m, and I-131, respectively. Total, the best-fit calculation for the $\sigma\gamma_{Te130\rightarrow Te131}$ and $\sigma\gamma_{Te130\rightarrow Te131m}$ cross-sections were 0.16 barns and 0.01 barns, respectively.

The residuals from each of the data points between the solved cross-section data set and the experiments were also compared and are expressed as a fraction of the experimental value as shown in Figures 3.9b, 3.10b, and 3.11b. The residual plots are simply for comparison on a per data point basis, meaning the x-axis was not scaled to fit the times when the data was collected. The residuals showed a decent fit between the Te-131m and I-131 data, but the Te-131 residuals showed an approximately 13% error in the initial data point calculations of the model. The residuals increased greatly for Te-131 and Te-131m towards the end of the data because the last few data points were collected between 100-350 hours post-irradiation, which was enough time and nearly enough time for the Te-131 and Te-131m to decay, respectively. Since the residuals are shown as a fraction of the experimental value, as the experimental value approached zero the error between the model and these values increased greatly.

When comparing the literature cross-section plot to the calculated cross-section and experimental data, it appeared that there was little discrepancy between any of them, except the Te-131m data. However, the calculated best-fit cross-section reduced the residuals considerably over the analytical result based on literature's cross-sections and demonstrates the code's ability to do perform the calculations. It is important to note that only the thermal flux and thermal cross-sections were considered in the literature-analytical cross-section calculation. Adding the higher energy cross-sections to the calculation that utilized literature cross-sections would increase the residuals between all the nuclides, whereas the least squares calculation, which the Monte Carlo method can be applied to, is capable of determining the averaged cross-section and fit it to the data directly, although this was not performed during the analysis of this work. Calculating the one-group averaged cross-section via least squares fitting could be beneficial to MURR because if an irradiation is performed in the same location in the reactor consistently, the calculated one-group cross-section would

help in predicting the final outcomes of the nuclides without having to know the average flux directly (assuming the energy distribution of neutrons remains stable over the fuel cycle). In summary, the calculation demonstrated the usefulness of the code's ability to calculate an averaged cross-section for a specific distribution for a repeated experiment.

The poor fit between the Te-131 experimental data and the calculated cross-section model could have been due to a lack of incorporating additional nuclides from the natural tellurium sample in the model, which could have resulted in the other elements contributing to the Te-131 yield. Alternatively, there could have been other experimental uncertainties or errors from MURR unknown to the author of this work, especially for the Te-131m data. The model appeared fit more towards the Te-131m data than Te-131 to minimize the squared residuals. Since the data appears erratic for Te-131m compared to those for Te-131 and I-131, and the total radiation emitted from the Te-131m was small, the high-purity germanium (HPGe) radiation detector used for this data may have had a difficult time measuring the radiation accurately, thus contributing additional uncertainty in the form of experimental error not considered by this work.

A correction in the model was not performed to fit the data better. The nonlinear model could have been adjusted by implementing additional variables to scale the Te-131 atoms down to the experimentally measured values, but due to the possibility of the previously described experimental error, the model was not adjusted. Other datasets of this same experiment may have aided in determining the discrepancy, but they were not performed or available.

Based on these results, the model appeared to fit the data acceptably. Thus, the Monte Carlo analysis was performed to incorporate known experimental and other parameter uncertainty to determine how the dependent $\sigma\gamma$ variables varied as functions of the input independent variables and to propagate the uncertainty through to the best-fit parameters. After iterating through the Monte Carlo analysis approximately 50,000 times, the code calculated the variables according to the distributions shown in the probability histograms in Figures 3.12a and 3.12b. Total, the code calculated an averaged $\sigma\gamma_{Te130\rightarrow Te131}$ cross-section of 0.4 $\pm$ 30 barns and a $\sigma\gamma_{Te130\rightarrow Te131m}$ cross-section of 0.02 $\pm$ 1 barns, for a total Te-130 (n, γ) cross-section of 0.46 $\pm$ 30 barns according to the formula shown in Equation 3.1. Since

the distribution is on a logarithmic scale, the larger calculated values greatly influenced the mean and standard deviation, which drove the uncertainty larger than the calculated mean value. After removing outliers from the data using quartiles, the averaged mean and standard deviation decreased to $6 \times 10^{-26} \pm 5 \times 10^{-26}\ cm^2$, which is smaller than the cross-sections reported in literature from Table 1.2. Neither the corrected nor uncorrected averages provided useful insight to the cross-section calculation.

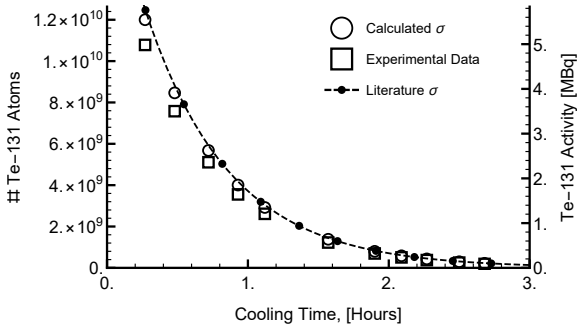

(a) Data and model comparison, Te-131

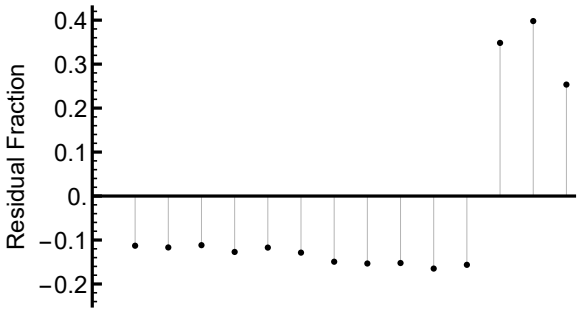

(b) Residual fraction, Te-131

Figure 3.9: Experimental data compared with the results from the model for Te-131.

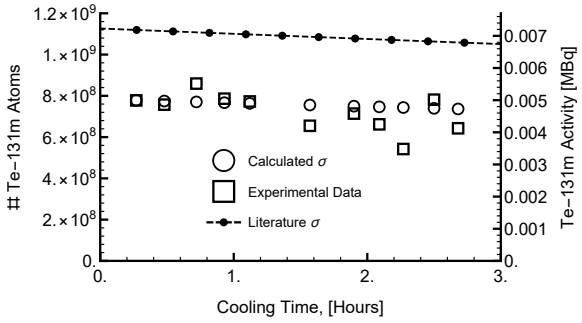

(a) Data and model comparison, Te-131m

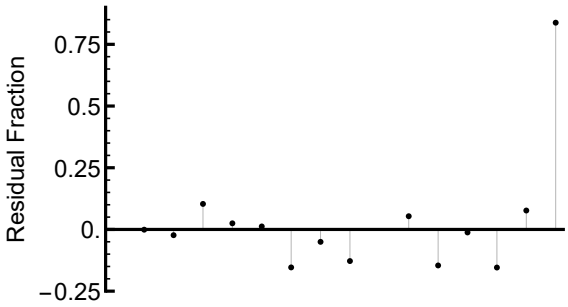

(b) Residual fraction, Te-131m

Figure 3.10: Experimental data compared with the results from the model for Te-131m.

The large uncertainty in this calculation was largely attributed to the log-scale variance in the cross-section, even after removing outliers. Surprisingly, the covariance matrix between the dependent and independent variables from the Monte Carlo analysis showed that there was no correlation between the resulting variables of interest and any of the other parameters entered into the system. In fact, there was not even a correlation coefficient above or below $+0.05$ or -0.05, respectively. There was also not a correlation between the sum of the

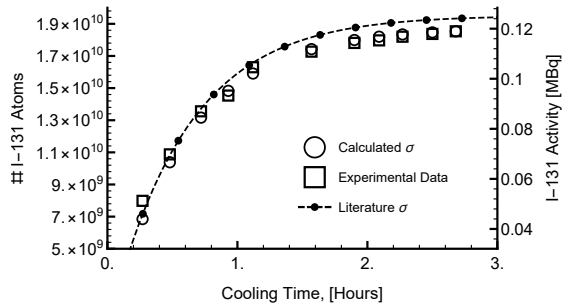

(a) Data and model comparison, I-131

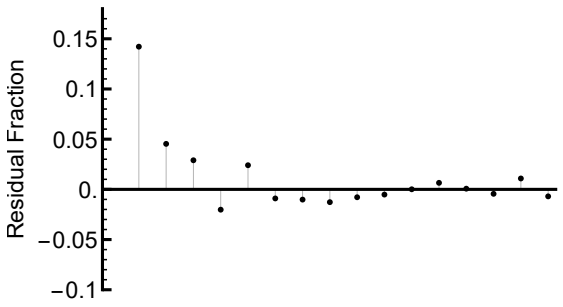

(b) Residual fraction, I-131

Figure 3.11: Experimental data compared with the results from the model for I-131.

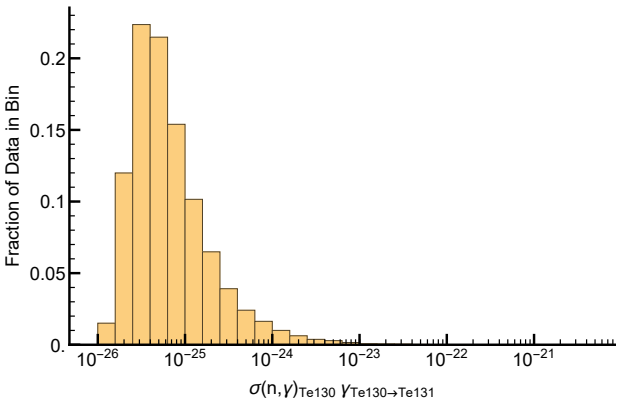

(a) Te-131

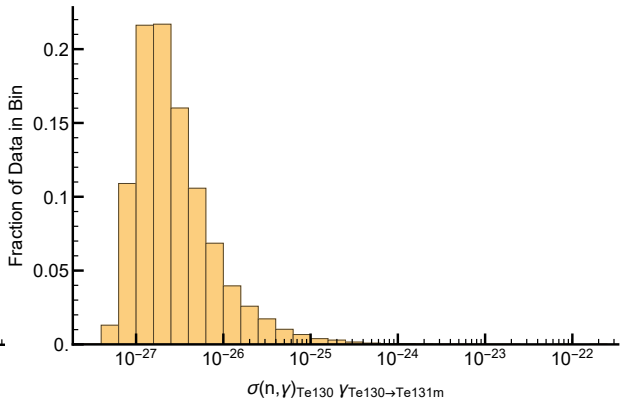

(b) Te-131m

Figure 3.12: Histograms of the calculated Te-130 neutron absorption cross-section times the fractional yield of Te-131 and Te-131m.

squared residuals and the parameters that the model performed the best-fit on. This could be related to the short irradiation time of this experiment and the resulting low yields of radioactivity in the measured nuclides, which could have increased the uncertainty in the measurements more than what this work accounted for. There was, however, a very strong correlation between the two independent $\sigma\gamma$ variables calculated during the analysis, which is shown in Figure 3.13. The code calculated the correlation coefficient between the two dependent $\sigma\gamma$ variables at essentially unity, 0.999.

The fractional yields of Te-131 and Te-131m calculated by the code during the Monte Carlo analysis according to Equations 3.2 and 3.3, respectively, resulted in normal distributions and are shown in Figures 3.14a and 3.14b. The normal distribution parameters were $\mu = 0.960$ and $\sigma^2 = 0.003$ for the fractional yield of Te-131 from Te-130 and $\mu = 0.040$

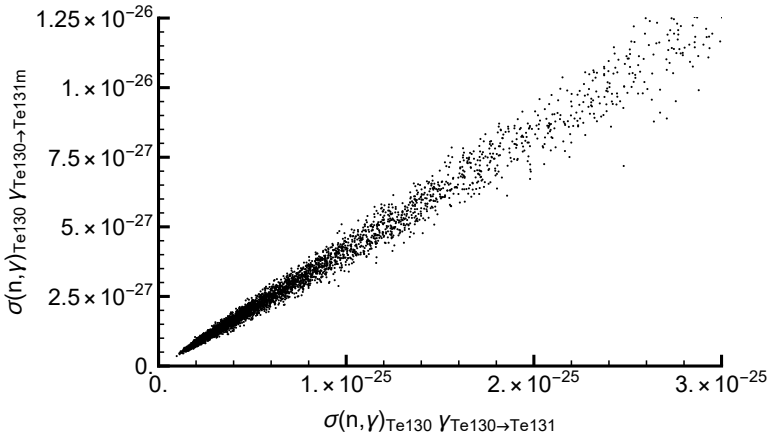

Figure 3.13: Sample data from the Monte Carlo analysis showing the covariance between the two variables from the second experiment.

and $\sigma^2 = 0.003$ for Te-131m from Te-130. The fractional yields were both very consistent across each of the Monte Carlo iterations. Although the variance in the cross-section from the Monte Carlo analysis was significantly larger than the average calculated cross-section, the surprisingly consistent results for the fractional yields provided exactly what this part of the analysis hoped to achieve–a calculated distribution of the fractional yields that could be used in elsewhere in this work.

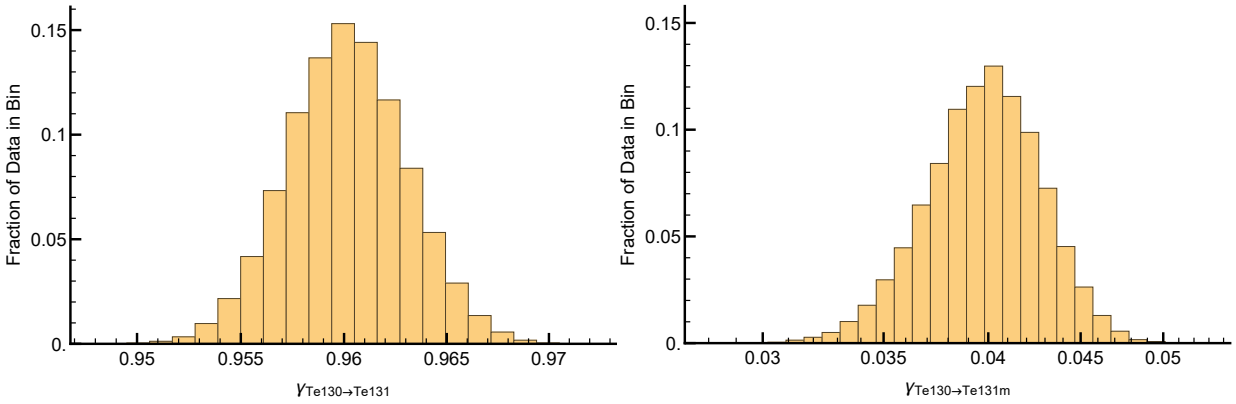

(a) Te-131 **(b)** Te-131m

Figure 3.14: Histograms of the calculated fractional yields of Te-131 and Te-131m.

3.2.2 Experiment 3

The same calculations from Section 3.2.1 were repeated using the data from the third MURR experiment. The results from the Monte Carlo analysis obtained from this experiment were not coherent. Again, the cross-section parameters fit by the average model matched the data well and better than the cross-section provided by literature, although both the curves are close to the experimental data as shown in Figure 3.15. The calculated best-fit parameters to the data from the averaged values for the experimental variables yielded 0.15 barns and 0.02 barns for the $\sigma\gamma_{Te130\rightarrow Te131}$ and $\sigma\gamma_{Te130\rightarrow Te13m1}$ cross-sections, respectively.

Averaged over the Monte Carlo calculations, the calculated Te-130 cross-section parameter was 0.15 $\pm$ 0.12 barns + 0.02 $\pm$ 0.12. As shown by the fitted curve in Figure 3.15, the average cross-sections fit the data well but the uncertainties attached to these values brought into question the validity of the calculation.

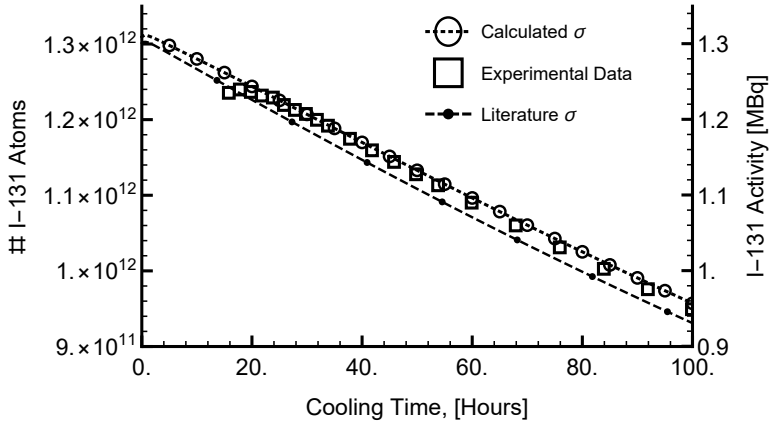

Figure 3.15: Average model fit of the cross-section parameters from the third MURR experiment.

Upon examining the data further, the inconsistencies between the iterations in the Monte Carlo method became clear. First, the covariance plot between the two independent cross-sections calculated by the code revealed that the iterative solutions often did not converge on real solutions, as shown in Figure 3.16. Second, the distributions calculated for the fractional yields of Te-131 and Te-131m were closer to uniform distributions from 0 to 1, which does not make sense, as shown in Figures 3.17a and 3.17b. This was probably due to the poor

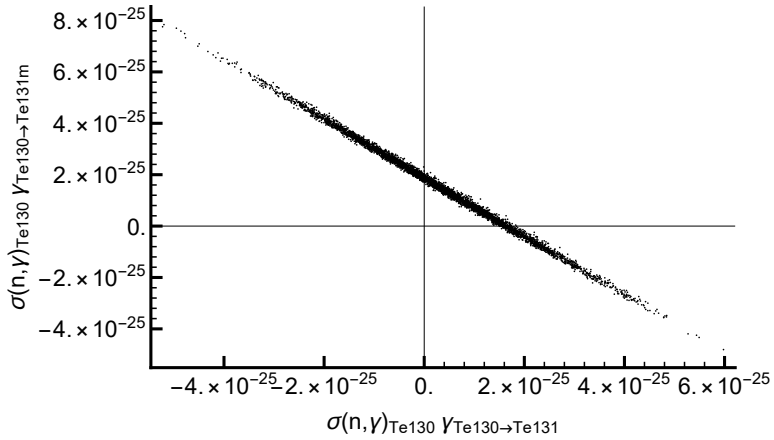

Figure 3.16: Sample data from the Monte Carlo analysis showing the covariance between the two variables for the third experiment.

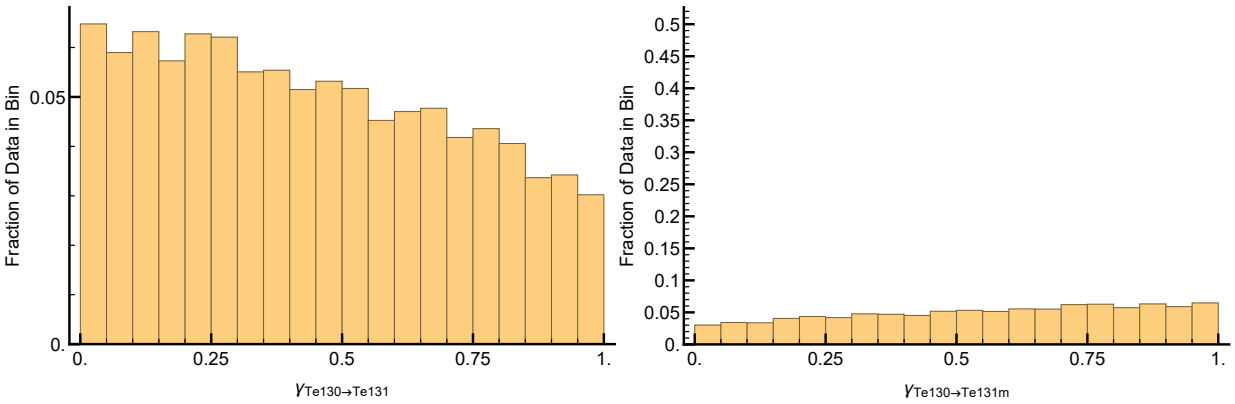

(a) Te-131 **(b)** Te-131m

Figure 3.17: Histograms of the calculated fractional yields of Te-131 and Te-131m.

data from MURR of the initial activity measurements, which showed an apparent peak of I-131 activity around 20 hours EOI (refer to the Experiment Data in Figure 3.15).

Finally, unlike the previous section, there was some correlation between the calculated independent variables and the I-131 yields, as would be expected. However, there was not significant correlation between any of the other variables in the system.

3.2.3 Experiment 1, Te-130 (n, γ) Cross-Section Only

The last set of experimental data that was used to fit parameters in the model was from the first MURR experiment. This experiment had a single measurement of the I-131 activity two hours following a 30 minute irradiation. As previously mentioned, this experiment utilized a much larger sample mass of TeO_2 than the other experiments of approximately 170.7 grams. Since only one equation was available for the code due to the lack of experimental data, only a single variable could be solved for per the stipulations imposed by the Gauss-Newton method and discussed in Section 2.3. Thus, the total neutron absorption cross-section of Te-130, $\sigma(n,\gamma)_{Te130}$, was computed by utilizing the fractional yields of Te-131 and Te-131m resulting from the Te-130 (n,γ) reaction from both literature and the distribution calculated in Section 3.2.1. Since the fractional yields varied widely in literature (refer to Table 1.2), a uniform distribution was chosen for the fractional yield of Te-131 from the neutron absorption reaction of Te-130 that varied between 0.9 and 1. The calculated distribution from Section 3.2.1 was normally distributed with parameters $\mu = 0.960$ and $\sigma^2 = 0.003$. The results from the two calculations were within the uncertainties of each other at 0.127 ± 0.008 barns (standard deviation of the mean of 2×10^{-5} barns following 226,000 calculations) and 0.125 ± 0.007 barns (standard deviation of the mean of 2×10^{-5} barns following 77,000 calculations) for the literature and calculated fractional yield distribution calculation sets, respectively. The fitted cross-section parameter followed a normal distribution in each of these calculations and the histograms are shown in Figure 3.18.

The smaller calculated cross-section from this experiment compared to the previous two sections was attributed to the neutron self-shielding of the larger sample. MURR modeled the TeO_2 target in the reactor using four neutron energy groups with the MONTEBURNS code and calculated that the approximately 170 gram TeO_2 target reduced the flux by a

factor of around 0.83, which is almost exactly the reduction calculated in this work from the best-fit parameters. This of course does not include the uncertainty calculated in the Monte Carlo calculations of the previous sections, only the best-fit data using the averaged experimental parameters.

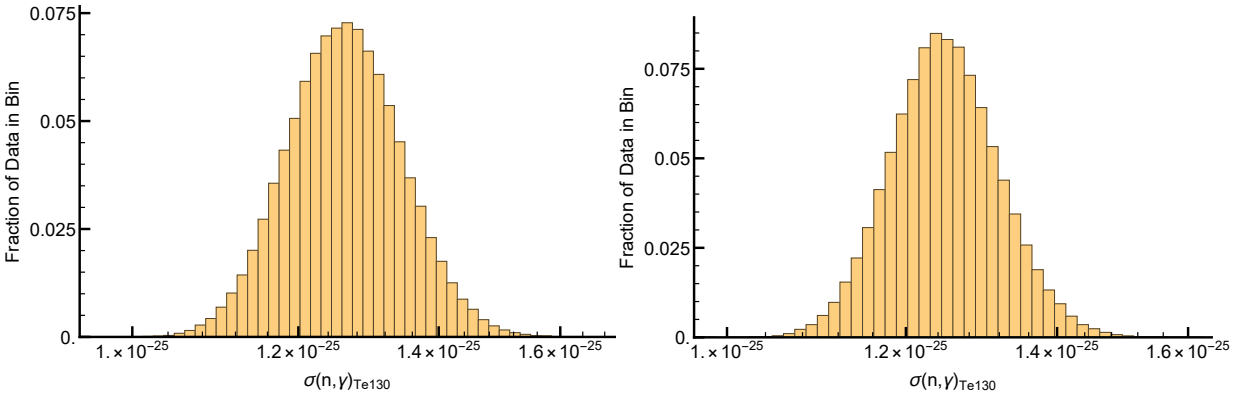

(a) Uniform distribution from literature **(b)** Calculated distribution

Figure 3.18: Histograms of the calculated Te-130 (n,γ) cross-section from Monte Carlo calculations that used distributions of the fractional yields of Te-131 and Te-131m from literature and Section 3.2.1.

Unlike the other sets of best-fit calculations performed by the Monte Carlo code, the computed variances in this calculation were logical. The covariance matrix yielded correlations between the system variables and calculated cross-section that would be expected and are shown in Table 3.2, unlike the calculations from the other two calculations experiments. Intuitively, the calculated cross-section should have a negative correlation with the neutron flux, since a larger cross-section would be required to produce the same nuclide activity and compensate for a smaller flux. This was clearly the case in this calculation set since the correlation coefficient was -0.8. The covariance matrix also revealed correlations between the calculated number of atoms of Te-131 and Te-131m, and the experimental I-131 measurement.

Lastly, the covariance matrix also showed a -0.48 and 0.48 correlation coefficient between the cross-section and the fraction yields of Te-131 and Te-131m, respectively, that result from the Te-130 (n,γ) reaction. As the fractional yield of Te-131 increased, the resulting I-131 activity at two hours post-irradiation also increased, which forced the best-fit cross-section

to decrease. Likewise, a decrease in the fraction yield of Te-131 resulted in an increase in the fractional yield of Te-131m, which ultimately resulted in a decreased final yield of I-131.

Table 3.2: Correlation coefficients between the calculated Te-130 (n,γ) cross-section and other system parameters computed from the Monte Carlo analysis for the first experiment

Descriptor	Variable	Correlation Coefficient
Flux	ϕ	-0.80
Te-131 Atoms	N_{Te131}	0.28
Te-131m Atoms	N_{Te131m}	0.59
I-131 Atoms	N_{I131}	0.34
Fractional Yield Te-131	$\gamma_{Te130 \rightarrow Te131}$	-0.48
Fractional Yield Te-131m	$\gamma_{Te130 \rightarrow Te131m}$	0.48

3.3 Validation

In addition to the three experimental test runs, MURR also provided experimental data for one full test (Experiment 4) that replicated the process they plan to use during full scale production of I-131. The data from this experiment was used in the code of this work to validate the assumptions, fractional yield distributions of Te-131 and Te-131m, and calculated Te-130 (n, γ) cross-section from the previous sections.

In this experiment, MURR irradiated a 173.6 gram sample of TeO_2 four separate and different times with various cooling times in between the irradiations. The thermal neutron fluxes and lengths or irradiation and cooling times are shown sequentially in Table 3.3. At the end of the eighth period (a ten hour cooling period), MURR extracted the I-131 from the rest of the tellurium sample and measured a final activity of 24.58 Ci (909.5 GBq) of I-131, or 0.1416 Ci per gram TeO_2 (5.239 GBq per gram TeO_2). Since MURR extracted the I-131 from the sample, it was difficult to determine the recovery yield of the I-131. MURR estimated that the recovery yield was approximately $\pm$ 5%.

Since the sample mass was very close to Experiment 3's mass, the calculated cross-section of 0.127 $\pm$ 0.008 barns from Experiment 3 was used without considering other self-shielding effects. Additionally, the Gauss-Newton iterative procedure was not required for this analysis

because variables of interest were simply the yields of the nuclides in the system, which the code calculated analytical derivations for per the method of residues, as previously discussed (refer to Chapter 2). The Monte Carlo method was employed using the uncertainties for the system parameters provided in literature, uncertainties in the experimental conditions provided by MURR (± 5% for the fluxes and ± 0.01 hours for the period time), a Te-130 (n, γ) cross-section chosen according to the normal distribution previously calculated, and finally the Te-131 and Te-131m fractional yields chosen according to their calculated distributions over 111,000 histories. The final result from the Monte Carlo calculation was a final I-131 yield of 920 ± 60 GBq (5.3 ± 0.4 GBq per gram TeO_2), which was well within the error of the measured activity by MURR. The results from the Monte Carlo calculations are shown in Figures 3.19, 3.20, and 3.21 for Te-131, Te-131m, and I-131, respectively.

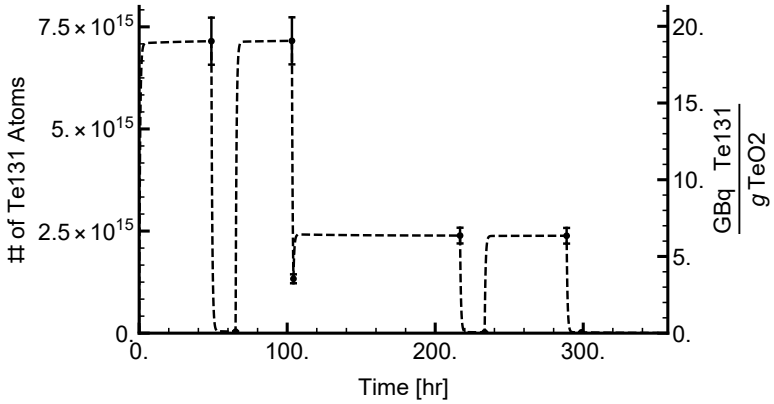

Figure 3.19: Analytical calculation for Te-131 with means and standard deviations from the Monte Carlo calculation shown at the end of each cooling or irradiation period.

Table 3.3: Experiment 4 (full-test) parameters

Time Period	Length	Thermal Flux
1	48.78 hours	9.9×10^{13} n·cm^{-2}·s^{-1}
2	16.38 hours	0
3	38.03 hours	9.9×10^{13} n·cm^{-2}·s^{-1}
4	1.03 hours	0
5	112.55 hours	3.29×10^{13} n·cm^{-2}·s^{-1}
6	16.63 hours	0
7	55.37 hours	3.29×10^{13} n·cm^{-2}·s^{-1}
8	10.00 hours	0

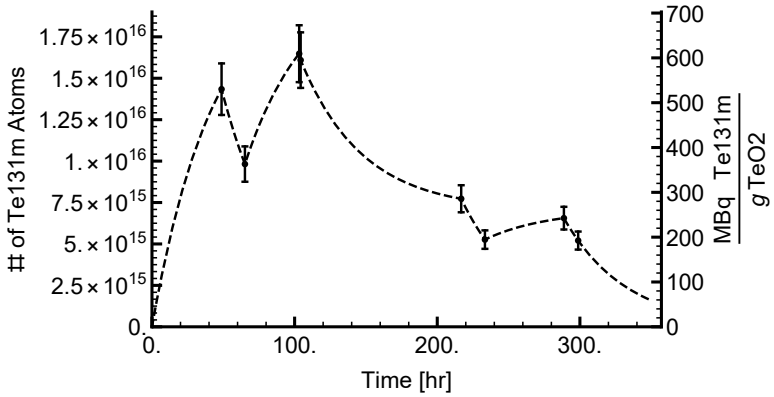

Figure 3.20: Analytical calculation for Te-131m with means and standard deviations from the Monte Carlo calculation shown at the end of each cooling or irradiation period.

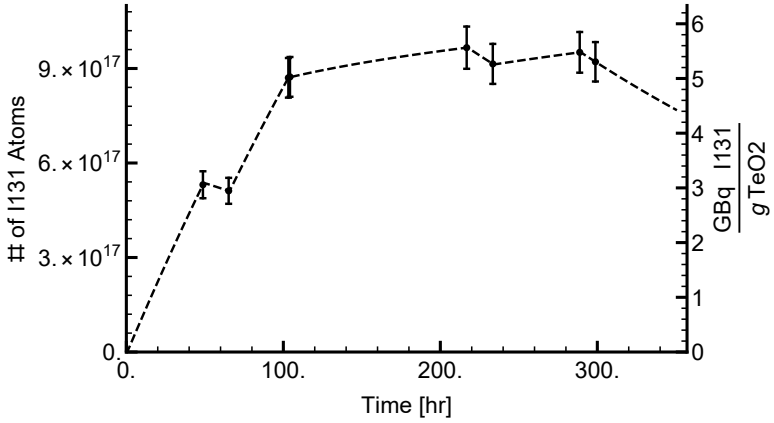

Figure 3.21: Analytical calculation for I-131 with means and standard deviations from the Monte Carlo calculation shown at the end of each cooling or irradiation period.

As seen in Figure 3.19, the Te-131 activity peaked and dropped to zero almost immediately during and following each of the irradiations. The neutron flux also influenced the peak activity significantly–about the same as the ratio in the change of fluxes (approximately one-third) between the irradiation periods. The flux and irradiation periods were not long enough for the Te-131m and I-131 activities to reach steady-state. Also, each of the nuclide's peak activity following irradiation and the data point with the uncertainties that represents the end of a period were indistinguishable. The Te-131 and Te-131m nuclide's activities began decreasing immediately following the end of irradiation, while the Monte Carlo analysis determined that the peak I-131 activity following the final irradiation period before processing was 0.11 ± 0.03 hours.

3.4 Optimal Cooling Time

The optimal cooling time to produce the maximum I-131 activity is highly debated in literature and the conclusions drawn for the optimal cooling time appear to have little to no mathematical backing (refer to Section 1.3). The optimal cooling time in Experiments 2 and 3 performed by MURR in this work showed that the optimal cooling times varied between approximately three hours and 20 hours, respectively. However, the derivative of the analytical solution in the full-test Experiment 4 showed that the optimal cooling time was as low as 0.11 hours. As previously discussed, the first few data points from Experiment 3 that resulted in an observed peak of I-131 activity at 20 hours post-EOI most likely had an unaccounted for experimental or measurement error. There was not another data set or calculation performed in this work that suggested an optimal cooling time of that length.

To calculate the optimal cooling time as a function of the irradiation time, the Monte Carlo code was arranged to run with the irradiation and cooling times set as symbolic variables in order to derive an analytical solution to the I-131 activity with the times set as variables. This calculation used the same uncertainties from literature for the decay constants and applied the distributions calculated in this work for the fractional yields of Te-131 and Te-131m as well as the Te-130 (n,γ) cross-section. The neutron flux was also set to 1×10^{14} n·cm^{-2}·s^{-1}across a 170.1 gram TeO_2 sample. Each Monte Carlo simulation acquired the analytical solution for I-131 in terms of the irradiation and cooling time variables. The irradiation time was then varied between 0.001 and 1×10^5 hours and the derivative of the remaining function was taken with the cooling time set as the variable. The code then solved for the cooling time in this derivative to determine the optimal cooling time to produce the largest I-131. The results are shown in Figure 3.22.

Since the distributions for the fractional yields and Te-130 (n,γ) cross-section from this work are approximate and based off of a experimental results, a secondary x-axis was constructed for varying conditions. The optimal cooling time was determined to be a function of the Te-130 cross-section, neutron flux, and irradiation time. Although the sample mass also plays a role, the underlying causes in changes to the optimal cooling time as a function of the sample mass can be attributed to increased self-shielding, which coincidentally can be

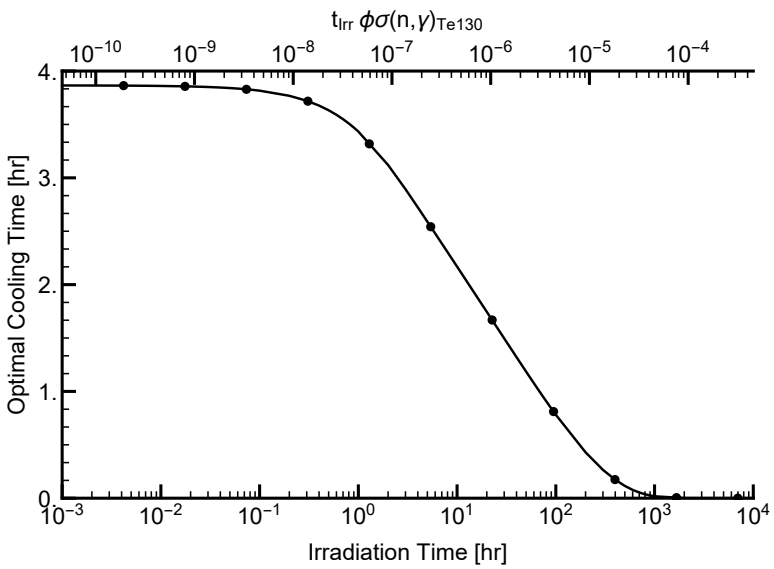

Figure 3.22: The optimal cooling time as a function of the irradiation time

summarized by the averaged neutron flux times the Te-130 cross-section across the sample. Additionally, the neutron absorption cross-sections of the other nuclides have been shown not to contribute to the final yields (refer to Section 3.1). Thus, if one is able to compute the average flux and cross-section across a sample for an irradiation case of a known time, the secondary x-axis of Figure 3.22 can be used to determine the optimal cooling time.

The Monte Carlo calculation showed that the optimal cooling time never exceeds 3.87 $\pm$ 0.02 hours for a very short irradiation. This was expected based on the large fractional yield of Te-131 from Te-130 and Te-131's very short half-life. The Te-131 decays very quickly into I-131, then the I-131 begins to decay and lose more atoms than what the Te-131m can contribute. As the I-131 activity reaches steady-state during irradiation, the optimal cooling time falls to essentially zero. Thus, the TeO_2 sample should be processed as soon as possible following irradiation to acquire the maximum amount of I-131.

There are other factors that need to be considered in addition to the optimal cooling time to produce the maximum I-131 activity. This analysis only considered four nuclides in the system, however other elements in the TeO_2 sample produce unwanted nuclides that may be extracted with the I-131 during processing. In reality, a processing facility may plan to wait a few hours in order to allow short-lived impurity nuclides to decay.

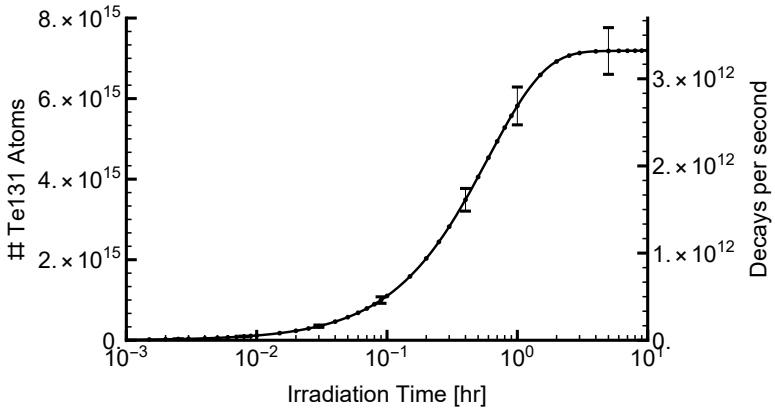

Figure 3.23: The number of Te-131 atoms and contribution to I-131 as a function of the irradiation time

3.5 Te-131 and Te-131m Activity Contribution

As has been discussed many times throughout this work, the contribution of atoms from Te-131 to I-131 is significantly larger than that of Te-131m. This is attributed to the fractional yield of Te-131 being larger than that of Te-131m (approximately 96% to 4%, as was calculated in Section 3.2 and seen in literature) and the half-life being significantly shorter (25.0 minutes to 33.25 hours), which results in a faster contribution of atoms from Te-131. To show this visually, the same Monte Carlo data from Section 3.4 was used to calculate the number of atoms of Te-131, Te-131m, and I-131, and plots of the number of atoms and contribution rates to I-131 were generated and are shown in Figures 3.23, 3.24, and 3.25, respectively. The contribution in decays per second for Te-131 and Te-131m are shown on the secondary y-axis. The number of Te-131 and Te-131m atoms during irradiation has a linear relationship to the product of the irradiation time, thermal neutron flux, and fractional yield of Te-131 and Te-131m from Te-130. The uncertainties shown are the standard deviations from the Monte Carlo analysis, not the estimate of the means.

This data was reproduced in Figure 3.26 to show the fractional contributions of the number of atoms per second from Te-131 and Te-131m to I-131. This data showed that even after Te-131m had reached its steady-state maximum number of atoms, it's contribution to the total number of I-131 atoms was still less than 4%. The uncertainty in the Monte Carlo analysis for this data varied with the fractional yield distribution. The uncertainty in the fractional yields was negligible and not visually reproducible on the plots.

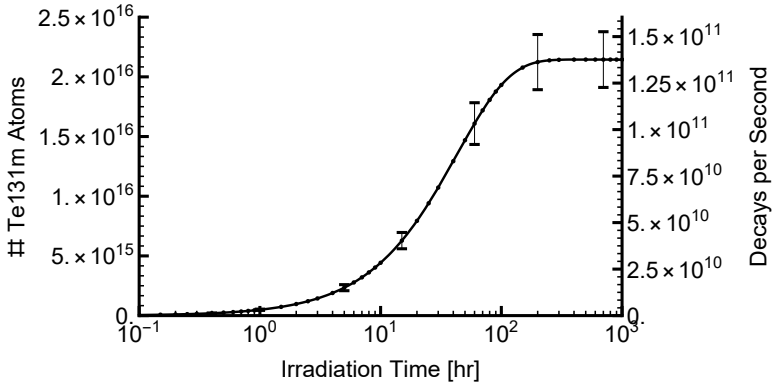

Figure 3.24: The number of Te-131m atoms and contribution to I-131 as a function of the irradiation time

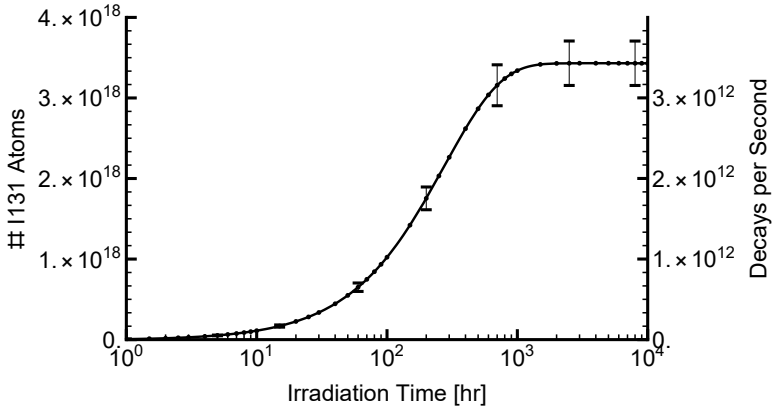

Figure 3.25: The number of I-131 atoms as a function of the irradiation time.

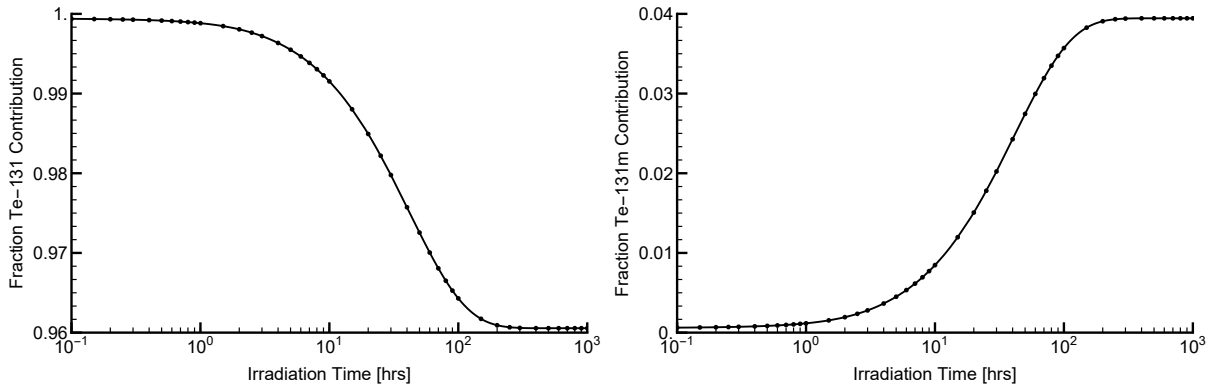

(a) Te-131 **(b)** Te131m

Figure 3.26: Fractional contributions of atoms per second from Te-131 and Te-131m to I-131

Chapter 4

Conclusions

MURR plans to begin commercial production of I-131 by irradiating a natural tellurium target that is partly comprised of Te-130 and acquiring the I-131 from the beta decay of the subsequent daughters of the Te-130 (n,γ) reaction, Te-131 and Te-131m. There are discrepancies in literature concerning many of the process variables, which makes it difficult to accurately predict the end yield and construct a process that maximizes the amount of I-131 generated. The analytical model constructed in this work took advantage of a symbolic computing language (Mathematica, [Inc.]) to solve a one-energy group model of the rate equations that govern the I-131 production process. The model provided solutions to the number of atoms of the nuclides in the system by linearly transforming the differential rate equations, combining the equations into matrix form, performing various matrix operations using Gaussian elimination, then calculating the inverse Laplace transform of the solutions via Cauchy's residue theorem. To evaluate other parameters in the system besides the amount of the nuclides, the code used the Gauss-Newton algorithm on the solution to the solved system of equations to perform a non-linear least squares fit of the parameters of interest using experimental data provided by MURR. A Monte Carlo analysis was used to evaluate the variance and covariance matrices in the various calculations based on user defined inputs for uncertainties of specific variables. The entire analysis focused only on thermal energy neutrons.

First, the analysis showed that the (n, tot) cross-sections of Te-131, Te-131m, and I-131 do not significantly influence the activities of the nuclides outside the error of the model. For

the remainder of the analysis, the cross-sections from literature were used for these variables. Following the elimination of these seldom studied cross-sections from the system, the Gauss-Newton method was used in the Monte Carlo analysis to determine functional estimates of the Te-130 (n, γ) cross-section and the fractional yields of Te-131 and Te-131m that result from the reaction. These parameters were best fit to the average experimental data that utilized small TeO_2 targets to yield 0.16 + 0.01 barns ($\sigma\gamma_{Te130 \rightarrow Te131} + \sigma\gamma_{Te130 \rightarrow Te131m}$) and 0.15 + 0.02 barns from Experiment 2 and 3, respectively. These parameters were also best-fit over each of the Monte Carlo histories but the results for each were not coherent. Despite this, the fractional yield parameters were very consistent for one of the experimental data sets and yielded normal distributions of 0.960 $\pm$ 0.003 and 0.040 $\pm$ 0.003 for Te-131 and Te-131m, respectively. These results correlate well with calculated fractional yields from nuclear databases. Successive comparisons of Monte Carlo calculations that used the calculated fractional yields and fractional yields from literature were within the errors of each other.

A third MURR experiment that utilized a larger, production sized TeO_2 target was used to determine the best-fit Te-130 (n, γ) thermal cross-section. The results from this Monte Carlo method were far superior to those obtained from the other MURR experiments. The best-fit cross-section was calculated to be 0.125 $\pm$ 0.007 barns. The decrease from the previous average best-fit model cross-section calculations from the other MURR experiments to this calculation (0.17 to 0.125) coincided well with MURR's calculation to account for the self-shielding of a larger sample.

The calculated parameters from the analysis were then validated in the model by comparing the code's analytical calculations against a final MURR experiment. In this final experiment, MURR irradiated a production sized sample four different times in various thermal neutron fluxes. MURR measured a final I-131 activity of 5.24 $\pm$ 0.26 GBq/g TeO_2 and the model determined the final activity to be 5.3 $\pm$ 0.4 GBq/g TeO_2 , well within the error or the actual yield. After validating the model and calculated parameters, the code was used to build an analytical solution as a function of the irradiation and cooling times of the TeO_2 target to determine the optimal cooling time of the sample to yield the largest amount of I-131. Despite the various claims of lengthy optimal cooling times in literature,

the optimal cooling time calculated via a Monte Carlo analysis never exceeded 3.87 ± 0.02 hours. The optimal cooling time maximum appeared as the irradiation time approached zero and the optimal cooling time decreased to zero the irradiation time increased. For the parameters of the system, this time was approximately 1000 hours of irradiation, which was when the I-131 activity reached steady-state.

In the future, the analysis should be redone for the averaged one-group or multi-group neutron energies. Although there is little indication that neutrons with energies above the thermal region significantly contribute to the I-131 production process, the cross-section and fractional yield parameters averaged over the entire neutron spectrum would provide a better functional estimate for various positions at MURR or at other reactors.

Also, if additional nuclide activity data were collected from the MURR experiments (Xe-131 activity, Te-132, for example), the system could be expanded and the code may be capable of finding functional estimates to the Te-131, Te-131m, and I-131 (n, γ) cross-sections. Although the cross-sections were shown not to influence the calculations outside of the uncertainty of the model, knowledge of these cross-sections would provide quality experimental information to these seldom studied nuclides.

It may be possible to expand the model to incorporate a full transport solution instead of using the simplified rate equations. The current set of equations does not consider fission or other changes in neutrons across the sample. Additionally, the code does not currently evaluate targets over their geometry, it simply uses the average flux across the sample. Incorporating this into the code may be beneficial, assuming the equations can still be derived analytically.

Bibliography

[1] (2006). Evaluated nuclear data file. 5, 30, 31

[2] (2006). Joint evaluated nuclear data file. 5

[3] (2014). Joint evaluated fission and fusion file, incident-neutron data. 2, 5

[4] Alanis, J. and Navarrete, M. (1999). Optimal parameters to produce 131i by neutron irradiation and melting of sintered tellurium dioxide. *Nuclear Instruments and Methods in Physics Research Section A: Accelerators, Spectrometers, Detectors and Associated Equipment*, 422(1):10 – 15. 10

[5] Alanis, J. and Navarrete, M. (2001). Industrial production of 131i by neutron irradiation and melting of sintered teo2. *AIP Conference Proceedings*, 576(1):853–856. 9, 10

[6] BAO, Z., BEER, H., KPPELER, F., VOSS, F., WISSHAK, K., and RAUSCHER, T. (2000). Neutron cross sections for nucleosynthesis studies. *Atomic Data and Nuclear Data Tables*, 76(1):70 – 154. 5

[7] Chapra, S. C. (2012). *Applied Numerical Methods with MATLAB®for Scientists and Engineers*. MCGraw-Hill, 3rd edition. 22

[8] El-Absy, M., El-Garhy, M., El-Amir, M., Fasih, T., and El-Shahat, M. (2010). Separation and purification of 131i from neutron irradiated tellurium dioxide targets by wet-distillation method. *Separation and Purification Technology*, 71(1):1 – 12. 10, 11

[9] Hershman, J. M. and Geffen, D. (2016). Thyroid cancers. 2

[10] Honztko, J., Konen, K., Kosina, Z., Becvar, F., and A. Eissa, E. (1984). A determination of the130te thermal neutron capture cross section. 34. 5

[Inc.] Inc., W. R. Mathematica, Version 11.2. Champaign, IL, 2017. 12, 14, 55, 67

[12] Khazov, Y., Mitropolsky, I., and Rodionov, A. (2006). Nuclear data sheets for a = 131. *Nuclear Data Sheets*, 107(11):2715 – 2930. 63

[13] Kochnov, O., Kolesov, V., Fomin, R., and Jerdev, G. (2015). Assessment of the increasing in 131-i production due to improved tellurium target in the wwr-c reactor core. *Nuclear Energy and Technology*, 1(3):213 – 217. 5, 6

[14] Mohamed, M. A. I. (2010). Radiochemical studies on the separation of iodine-131 and radioiodination of some organic coumpounds. Master's thesis, Benha University. 11

[15] Mostafa, M. (2009). Radioactivity calculations for production of 131i by neutron irradiation of tellurium targets. *Radiochemistry*, 51(3):313–320. vii, 6, 7, 8, 9

[16] Mughabghab, S. F. (2006). *Atlas of Neutron Resonances: Resonance Parameters and Thermal Cross Sections. Z=1-100*. Elsevier, 5th edition. 5

[17] N, H., AM, N., M, K., D, M., K, B., CL, K., M, Y., J, R., Z, T., A, M., DR, L., HS, C., EJ, F., and KA, C. (1975-2014). Seer cancer statistics review, 1975-2014, national cancer institute. bethesda, md. based on november 2016 seer data submission, posted to the seer web site, april 2017. 2

[18] NUREG/CR-4884 (1988). *Interpretation of Bioassay Measurements*. Brookhaven National Laboratory, Long Island, New York. 2

[19] Rivkees, S. A., Sklar, C., and Freemark, M. (1998). The management of graves disease in children, with special emphasis on radioiodine treatment. *The Journal of Clinical Endocrinology and Metabolism*, 83(11). 2

[20] Smith, C. L. (1978). The isotopic composition of tellurium. *International Journal of Mass Spectrometry and Ion Physics*, 28(1):7–17. vii, 3

[21] Survey, U. G. (2017). Mineral commodity summaries 2017: Us geological survey. 3

[22] Tomandl, I., Honzátko, J., von Egidy, T., Wirth, H.-F., Belgya, T., Lakatos, M., Szentmiklósi, L., Révay, Z., Molnár, G. L., Firestone, R. B., and Bondarenko, V. (2003). Thermal neutron capture cross sections of tellurium isotopes. *Phys. Rev. C*, 68:067602. 5

[23] TUNBRIDGE, W. M. G., EVERED, D. C., HALL, R., APPLETON, D., BREWIS, M., CLARK, F., EVANS, J. G., YOUNG, E., BIRD, T., and SMITH, P. A. (1977).

The spectrum of thyroid disease in a community: The whickham survey. *Clinical Endocrinology*, 7(6):481–493. 1

[24] Watson, K. M. (1952). The effect of final state interactions on reaction cross sections. *Phys. Rev.*, 88:1163–1171. 5

[25] Wedepohl, K. H. (1995). The composition of the continental crust. *Geochimica et Cosmochimica Acta*, 59(7):1217–1232. 3

Appendices

A Summary of Constants

A.1 Literature Constants and Uncertainties

The following table provides the constants from literature and their uncertainties, when available, that the model used in this work.

Table A.1: Summary of constants used in this work

Description	Value	Reference
Half-life, I-131	8.0252 ± 0.0006 days	[12]
Decay constant, I-131	$9.9967 \times 10^{-7} \pm 7 \times 10^{-11}$ seconds	–
Half-life, Te-131	25.0 ± 0.1 minutes	[12]
Decay constant, Te-131	$4.62 \times 10^{-4} \pm 0.02 \times 10^{-4}$ seconds	–
Half-life, Te-131m	33.25 ± 0.25 hours	[12]
Decay constant, Te-131m	$5.791 \times 10^{-6} \pm 0.004 \times 10^{-6}$ seconds	–
Fractional Decay Yield of I-131 from Te-131m	$74.1 \pm 0.5\%$	[12]
Fractional Decay Yield of Te-131 from Te-131m	$25.9 \pm 0.5\%$	[12]

A.2 MURR Experiment 1 Data and Uncertainties

The first MURR experiment involved a large 170.7 g TeO_2 sample irradiated for 30 minutes before a two hour cooling period. The target was homogenized in an HDPE bottle by vigorous shaking. The sample was taken for radioassay with an I-131 mass in the range of 0.5 to 0.7 grams. The total activity after the two hour cooling time was 0.879 ± 0.019 mCi/g TeO_2 . The total activity for the entire target was 150 ± 3.2 mCi. In addition to the uncertainties from the half-lives and fractional decay yields from Table A.1, the experimental uncertainties from Table A.2 were used in the Monte Carlo analysis.

Table A.2: Uncertainties from MURR Experiment 1 used in this work

Description	Value
I-131 Activity	150 ± 3.2 mCi
Irradiation Time	0.50 ± 0.01 hours
Cooling Time	2.00 ± 0.01 hours
Thermal Neutron Flux	$9.9 \times 10^{13} \pm 0.5 \times 10^{13}$ n·cm^{-2}·s^{-1}

A.3 MURR Experiment 2 Data and Uncertainties

The second MURR experiment involved the irradiation of a 0.1231 g TeO_2 sample for 10 seconds in a lower thermal neutron flux. MURR pneumatically conveyed the sample into the reactor for the short irradiation time. A HPGe semi-conductor detector measured the entire sample activity of I-131, Te-131, and Te-131m starting at 0.27 hours EOI and ending at 306.55 hours. The HPGe measured the activities with an accuracy of approximately ± 1%, although the uncertainty in the Te-131m was set higher since the activity was so small and the resulting measurement was unstable compared to that of I-131 and Te-131. In addition to the uncertainties from the half-lives and fractional decay yields from Table A.1, the experimental uncertainties from Table A.3 were used in the Monte Carlo analysis.

Table A.3: Uncertainties from MURR Experiment 2 used in this work

Description	Value
I-131 Activity	Various ± 1%
Te-131 Activity	Various ± 1%
Te-131m Activity	Various ± 2%
Irradiation Time	10.0 ± 0.1 seconds
Cooling Time	Various ±0.01 hours
Thermal Neutron Flux	$6.5 \times 10^{13} \pm 0.3 \times 10^{13}$ n·cm^{-2}·s^{-1}

A.4 MURR Experiment 3 Data and Uncertainties

The third MURR experiment utilized a very small 1×10^{-4} g sample of TeO_2 that was irradiated for 150 hours. At the end of the irradiation, a dose calibrator with an estimated accuracy of ± 2% measured the activity of the I-131 in the sample starting at EOI 14.6 hours to 171.4 hours. In addition to the uncertainties from the half-lives and fractional decay yields from Table A.1, the experimental uncertainties from Table A.4 were used in the Monte Carlo analysis.

Table A.4: Uncertainties from MURR Experiment 3 used in this work

Description	Value
I-131 Activity	Various $\pm$ 2%
Irradiation Time	150.00 ± 0.01 hours
Cooling Time	Various ± 0.01 hours
Thermal Neutron Flux	$9.8 \times 10^{13} \pm 0.5 \times 10^{13}$ n·cm^{-2}·s^{-1}

B Functions and Equations

This appendix retains code samples from the work and general equations used in the analysis.

B.1 Code Sample of Cauchy's Residue Theorem

The following Mathematica ([Inc.]) code sample was the code used to evaluate the inverse Laplace transform via Cauchy's residue theorem. Although complicated in descriptive nature, the actual implementation is concise. The code was capable of evaluating any number of matrices at time, and the NComps variable represents the number of matrices being evaluated at the current time. The solution to the rate equations from Gaussian elimination was first passed to the xCheckDimsFull function, which passed each element of each matrix to the xCheckDims function, where the code reduced the input to a single numerator and denominator. After this was completed, the matrix was passed to the xResidueFull function which again sent each part of the input matrix to a seperate function, xResidue, to be evaluated. This function calculated the sum of the residues by simplifying the expression's polynomials into simple terms. Refer to Section 2.1 for further description on the theory.

```
(*xCheckDimsFull takes the full matrix and cycles through all the
elements putting them into xCheckDims which changes them to only a
single numerator and denominator.*)
xCheckDims[MatrixPart_] :=
 Module[{xMatrixPart = MatrixPart, headtype, numden},
  headtype = Head[xMatrixPart];
  If[TrueQ[headtype == Plus],
   Table[
    xCheckDims[xMatrixPart[[i]]],
    {i, 1, Length[xMatrixPart]}],
   numden =
    Collect[Numerator[xMatrixPart], s]/
     Collect[Denominator[xMatrixPart], s]]]
```

```
xCheckDimsFull[Matrix_] := Module[{xMatrix = Matrix},
  Table[
  xCheckDims[Factor[xMatrix[[i, j]]]],
  {i, 1, NComps}, {j, 1, NLength}]]

(*Takes the entire matrix and plugs it in to the xResidue
function to calculate the inverse laplace transform via
residues.*)
xResidueFull[Matrix_] := Module[{xMatrix = Matrix},
   Table[
   xResidue[xMatrix[[i, j]], i],
   {i, 1, NComps}, {j, 1, NLength}]];

(*Calculates the inverse laplace transform using the method of
residues. This function works only for a single element in
the matrix*)
xResidue[MatPart_, NComp_] := Module[{xMatPart = MatPart, dims},
   dims =
    Dimensions[
        CoefficientList[Denominator[xMatPart], s]][[1]] -
     1;(*The power of the s in the denominator*)
   Total[
   Table[(((Numerator[xMatPart]/D[Denominator[xMatPart], s]) /.
           s -> #)*Exp[t[NComp]*#]) &@
      Root[Denominator[xMatPart] /. s -> # &, i], {i, 1, dims}]]
   ];
```

Vita

Robert Haffner works as a mechanical engineer in the electrical generation department of POWER Engineers, Inc.–a global multidisciplinary engineering firm that provides consulting services to a variety of industries. He received his undergraduate Mechanical Engineering degree from the University of Missouri–Columbia. As an undergraduate, Robert began research and graduate coursework through the Nuclear Science and Engineering Institute (NSEI) at the University of Missouri and, upon graduation, began working part-time at the University of Missouri Research Reactor (MURR) under Dr. William (Bill) Miller. While at MURR, Robert was introduced to the I-131 production process and began developing an in vivo monitoring program for the employees at the new I-131 production facility. He also began preliminary calculations to verify calculated yields of I-131 produced by the neutron activation of natural tellurium by MURR and discovered the inconsistencies literature presented of this process. During his time at MURR, Robert received and accepted an offer for a mechanical engineering position at a small design firm, Sega Inc., who was later acquired by POWER Engineers. He transferred his graduate credits from the NSEI to the University of Tennessee–Knoxville to complete his degree through online courses. Robert is married to Anna Haffner and they are expecting twins this summer.